



Modeling magnetic properties of actinide complexes

Hélène Bolvin

► To cite this version:

Hélène Bolvin. Modeling magnetic properties of actinide complexes. Computational Modelling of Molecular Nanomagnets, 34, Springer, pp.179-218, 2023, Challenges and Advances in Computational Chemistry and Physics, 978-3-031-31037-9. 10.1007/978-3-031-31038-6_5 . hal-03761147

HAL Id: hal-03761147

<https://hal.science/hal-03761147v1>

Submitted on 25 Aug 2022

HAL is a multi-disciplinary open access archive for the deposit and dissemination of scientific research documents, whether they are published or not. The documents may come from teaching and research institutions in France or abroad, or from public or private research centers.

L'archive ouverte pluridisciplinaire **HAL**, est destinée au dépôt et à la diffusion de documents scientifiques de niveau recherche, publiés ou non, émanant des établissements d'enseignement et de recherche français ou étrangers, des laboratoires publics ou privés.

Modeling magnetic properties of actinide complexes

Hélène Bolvin

Abstract This chapter presents different aspects of the modeling of magnetic properties in monomeric open-shell actinide complexes. Those properties are closely related to their electronic structure, which is difficult to achieve since none of crystal-field effects, electron-electron repulsion nor spin-orbit interaction is predominant. The electronic structure should be analyzed within the intermediate coupling scheme, between on one hand the Russell-Saunders coupling scheme where the inter-electronic repulsion is considered before spin-orbit, and, on the other hand, the j-j coupling scheme where one-electron wave-functions including spin-orbit are used to build the many-electron wave-function. Ab initio calculations on these complexes are challenging, and SO-CAS based methods are still the quantum chemistry tool of choice since they include a balanced description of the three effects. It is only by a close interplay between experimental data which are sparse for transuranide complexes due to radioactivity, numerical methods, and model Hamiltonians that one succeeds to unravel the electronic structure and magnetic properties of these complexes.

1 Electronic structure of actinide complexes

Most of the actinide compounds are man-made since the 20th century. Thorium and uranium are both long-lived and can be found in the earth in notable amounts. Actinium and protactinium exist in nature in extremely small amounts whereas transuranium elements are man-made. All the actinides are radioactive, quite strongly for some of them. This requires facilities specially equipped and approved for radioactive work. The radioactivity often plays a part in their chemistry and may impact their magnetic properties. The majority of the studies concern thorium and uranium compounds, particularly the latter, due to accessibility of raw materials, ease of han-

Hélène Bolvin
Laboratoire de Chimie et de Physique Quantiques, CNRS, Université Toulouse 3, France, e-mail:
bolvin@irsamc.ups-tlse.fr

Relativistic effects are more pronounced for actinides than for lanthanides, since their atomic number is larger. Scalar relativistic effects lead to an expansion and a destabilization of d and f orbitals. 5f orbitals in actinides are more destabilized than are the 4f orbitals of the lanthanides, to be nearly degenerate with the empty 6d and 7s orbitals for early actinides [2]. As a result, those valence orbitals are more chemically active, more valence electrons can be involved in the formation of compounds and a wider range of oxidation states is observed. Spin-orbit coupling leads to the splitting of the f orbitals; due to their small density close to the nucleus, this effect is not as important as for p orbitals, and actinide free ions are still well described within the Russell-Saunders coupling scheme, where the many-electron states are built at the spin-free level, and spin-orbit coupling calculated between many-electron states: the states of the free ion are accordingly labeled as $^{2S+1}L_J$, where L , S and J are the orbital, spin and total angular moments, respectively. This scheme is used when the electronic repulsion is greater than the spin-orbit splitting in contrast to j-j coupling where the spin-orbit coupling is introduced at the one-electron level. Since spin-orbit coupling is larger in actinides than in lanthanides, one needs to go beyond the Russell-Saunders coupling scheme, by mixing states with the same value of the total angular momentum J .

In this chapter, we will address the magnetic properties of molecular actinide systems, containing only one actinide center, with an open 5f shell. Magnetic properties probe the low lying states, up to thermal energy. The various multiplets of actinide complexes can not be described within a single-configuration framework. Scalar relativistic DFT (Density Functional Theory) methods are generally adequate for the calculation of the ground state properties of actinide systems, including molec-

ular geometries and vibrational frequencies [3, 4] but not suitable to describe the many excited states. Since there is not a clear predominance between the covalent effects, the electron repulsion nor the spin-orbit coupling in the 5f orbitals, all those interactions need to be adequately described, not only to achieve a quantitative but even a qualitative description. Scalar relativistic effects are easily incorporated using the non-relativistic machinery [5, 6]. SO-CAS (Spin-Orbit Complete Active Space) based methods [7] have been successfully applied to actinide complexes since one decade. In the first step, the CASSCF (Complete Active Space Self-Consistent Field) [8] method describes the multi-configurational many-electron states, which are corrected for dynamical correlation by a perturbative method, CASPT2 (Complete Active Space Perturbation Theory 2nd order) [9] or NEVPT2 (N-Electron Valence state Perturbation Theory 2nd order) [10] in a second step. The spin-orbit coupling is calculated as state interaction between those many-electron correlated wave functions in the last step [11]. This scheme is in line with the Russell-Saunders coupling scheme. To obtain a full treatment of the spin-orbit interaction, four-component methods should be used; but four-component multi-configurational correlated methods allow only the description of molecules with few atoms [12, 13]. The first-principle calculations are still challenging for actinide complexes, because they gather many of the difficulties of quantum chemistry: they are open-shell and should be described using multi-configurational methods as soon as there is more than one unpaired electron, relativistic effects are important, both scalar and spin-orbit, and correlation effects play an important role.

Magnetic properties of actinide complexes are mostly characterized by their magnetic susceptibility, either in solid state using a SQUID (Superconducting Quantum Interference Device) spectrometer which provides the average susceptibility and in a large temperature range, or in solution, using the Evans method, which probes by paramagnetic NMR (Nuclear Magnetic Resonance) a control molecule, usually around room temperature. On the other hand, paramagnetic NMR on nuclei of the ligand provides essential information about the susceptibility tensor, when the so-called dipolar contribution is dominant. We consequently devote the second Section to the modeling of the magnetic susceptibility. Magnetic properties are usually described using model Hamiltonians, using phenomenological parameters. For monomeric actinide complexes, the most used model Hamiltonians are the crystal-field Hamiltonian and spin Hamiltonians in degenerate or nearly-degenerate manifolds. This will be presented in the third Section of this chapter. Finally, we review shortly in the last Section recent works where magnetic properties of actinide complexes were modeled either based on *ab initio* calculations or on crystal-field theory.

2.1 Magnetic susceptibility tensor from ab initio calculations

(a) Note the difference between $\hat{\mathbf{m}}$ the magnetic moment operator, in units of μ_B (in SI J.T⁻¹) and $\hat{\mathbf{M}}$ the total angular momentum, in units of \hbar (in SI J.Hz⁻¹).

frame and values are deduced [14]. In general, the principal axes frame depends on temperature.

Most susceptibility measurements are performed on polycrystalline samples that give only the average susceptibility. Magnetic susceptibility values can also be performed on liquid solutions of pure compounds by use of the Evans nuclear magnetic resonance (NMR) method [15]. The average susceptibility is obtained by summing up on many directions equivalently distributed on the unity sphere

$$\chi = \frac{1}{4\pi} \int \chi_{uu} d\mathbf{u} \quad (5)$$

where \mathbf{u} is a unit vector. This is close to

$$\chi_M = \frac{1}{3} (\chi_{xx} + \chi_{yy} + \chi_{zz}) \quad (6)$$

The average magnetization as a function of the strength of the field is calculated along the same lines

$$\langle m(B) \rangle_T = \frac{1}{4\pi} \int \langle m_u(B_u) \rangle d\mathbf{u} \quad (7)$$

Contrarily to the magnetic susceptibility, which is calculated for small magnetic fields, $\langle m(B) \rangle_T$ might be very different from $\frac{1}{3} (\langle m_x(B_x) \rangle + \langle m_y(B_y) \rangle + \langle m_z(B_z) \rangle)_T$, in particular, at high field in the case of strong anisotropic response. As an example, in the case of an axial magnetic system with $\chi_x = \chi_y = 0$, at saturation, Eq. 7 leads to $\langle m(B) \rangle_T = \langle m_z(B_z) \rangle_T / 2$, instead of $\langle m_z(B_z) \rangle_T / 3$ for the previous equation.

In one word, the susceptibility and magnetization deduced from SO-CAS based calculations take into account the Zeeman interaction between the zero-field states to all orders, since the eigenstates of $\hat{\mathcal{H}}$ are calculated by diagonalizing the representation matrix of $\hat{\mathcal{H}}$ in the presence of the magnetic field. The limitation of the calculation is due to the approximate resolution for the eigenstates of $\hat{\mathcal{H}}^0$.

2.2 Generalized Van Vleck equation

The Van Vleck formula is commonly used to describe the susceptibility. But this implies to know a priori the principal axes frame of the χ tensor, which is not obvious for molecules lacking symmetry. A generalized formula has been derived for those cases [16, 17]. Due to Kramers' theorem, the energy levels of a system with an odd number of electrons are even-fold degenerate in the absence of magnetic field. In general, this degeneracy is two-fold, except for the cubic and icosahedral point groups where it might be four-fold and six-fold, respectively. In non-Kramers complexes, with an even number of electrons, the degeneracy arises from spatial symmetry. A non-degenerate state has no first-order magnetic contribution, according to Eq. A2

of the Appendix. It follows that in a non-symmetric molecule with an even number of electrons, magnetization only arises from second-order Zeeman interaction, the coupling by $\hat{\mathcal{H}}^Z$ between different energy levels.

$$\chi_{uv} = \mathcal{N}_A \mu_0 \mu_B^2 \frac{1}{Q^0} \sum_I e^{-\frac{E_I^0}{kT}} \left[\frac{1}{kT} \sum_{\iota, \iota'} \langle I, \iota | \hat{M}_u | I, \iota' \rangle \langle I, \iota' | \hat{M}_v | I, \iota \rangle \right. \\ \left. + 2 \sum_{K \neq I} \sum_{\iota, \kappa} \frac{\text{Re} \left(\langle I, \iota | \hat{M}_u | K, \kappa \rangle \langle K, \kappa | \hat{M}_v | I, \iota \rangle \right)}{E_K^0 - E_I^0} \right] \quad (8)$$

$$E_I = E_I^0 - \mu_B M_{I,u}^0 B_u + \mu_B^2 X_{I,u}^0 B_u^2 + \dots \quad (9)$$

$$\chi = \frac{\mathcal{N}_A \mu_0 \mu_B^2}{3} \sum_{u=x,y,z} \frac{\sum_I \left(\frac{(M_{I,u}^0)^2}{2kT} - 2X_{I,u}^0 \right) e^{-\frac{E_I^0}{kT}}}{\sum_I e^{-\frac{E_I^0}{kT}}} \quad (10)$$

Eq. 8 can be rewritten in a more compact form introducing the matrix representation M_u of \hat{M}_u in the basis of the zero-field states $|I, \iota\rangle$. One gets

where $\sum_{\iota, \kappa} \langle I, \iota | \hat{M}_u | K, \kappa \rangle^2 = \|\mathbf{M}_{u, IK}\|^2$ denotes the norm of the matrix. The sum runs now over the degenerate manifolds of the zero-field Hamiltonian.

It is instructive to consider only two manifolds of respective degeneracies d_1 and d_2 , separated by a zero-field energy gap ΔE . In this case, Eq. 11 becomes

$$\chi_{uu} = \mathcal{N}_A \mu_0 \mu_B^2 \frac{1}{d_1 + d_2 e^{-\frac{\Delta E}{kT}}} \left[\frac{\|\mathbf{M}_{u,1}\|^2}{kT} + \frac{e^{-\frac{\Delta E}{kT}} \|\mathbf{M}_{u,2}\|^2}{kT} + \frac{2 \left(1 - e^{-\frac{\Delta E}{kT}}\right) \|\mathbf{M}_{u,12}\|^2}{\Delta E} \right] \quad (12)$$

Let us now consider the two limit cases:

- the second manifold is not populated $\Delta E \gg kT$, $e^{-\frac{\Delta E}{kT}} \approx 0$

$$\chi_{uu} = \frac{\mathcal{N}_A \mu_0 \mu_B^2}{d_1} \left(\frac{\|\mathbf{M}_{u,1}\|^2}{kT} + \frac{2 \|\mathbf{M}_{u,12}\|^2}{\Delta E} \right) \quad (13)$$

the first term is the $1/T$ Curie term arising from the ground manifold, and the second term is the temperature independent paramagnetic (TIP) term, arising from the coupling with the non-populated manifold.

- the case where the energy gap is much smaller than the thermal energy, the two states are equally populated $\Delta E \ll kT$, $e^{-\frac{\Delta E}{kT}} \approx 1 - \frac{\Delta E}{kT}$

$$\chi_{uu} = \mathcal{N}_A \mu_0 \mu_B^2 \left[\frac{\|\mathbf{M}_{u,1}\|^2 + \|\mathbf{M}_{u,2}\|^2 + 2 \|\mathbf{M}_{u,12}\|^2}{(d_1 + d_2) kT} + \frac{\left(d_2 \|\mathbf{M}_{u,1}\|^2 - d_1 \|\mathbf{M}_{u,2}\|^2 + (d_2 - d_1) \|\mathbf{M}_{u,12}\|^2 \right) \Delta E}{4 (d_1 + d_2)^2 (kT)^2} \right] \quad (14)$$

The first term corresponds to the limit $\Delta E = 0$; the two manifolds merge together. One gets a $1/T$ Curie term for the $1+2$ manifold, $\|\mathbf{M}_{u,1}\|^2 + \|\mathbf{M}_{u,2}\|^2 + 2 \|\mathbf{M}_{u,12}\|^2$ is nothing more than $\|\mathbf{M}_{u,1+2}\|^2$. It is interesting to note that despite the fact that Eq. 11 arises from a perturbative treatment of the Zeeman interaction, and the difference of energy appears in the denominator of the Van Vleck term, when this energy gap vanishes, the equations are still valid, because $\left(e^{-\frac{E_K^0}{kT}} - e^{-\frac{E_I^0}{kT}} \right) / (E_K^0 - E_I^0)$ tends to $1/kT$ when $E_K^0 - E_I^0$ vanishes. When the gap ΔE is of the order of magnitude of the thermal energy, the further $1/T^2$ term describes the change of population of the second manifold.

χT as a function of T is represented in Fig. 1 in the case of two Kramers doublets for different values of $\|\mathbf{M}_1\|^2$, $\|\mathbf{M}_{12}\|^2$, $\|\mathbf{M}_2\|^2$ and ΔE . It reveals very different behaviors. For $\Delta E = 40 \text{ cm}^{-1}$, the plateau is reached at room temperature, and its height depends on the sum of $\|\mathbf{M}_1\|^2$, $\|\mathbf{M}_{12}\|^2$, $\|\mathbf{M}_2\|^2$ (see Eq. 14). When $\|\mathbf{M}_1\|^2 > \|\mathbf{M}_2\|^2$, there is small decrease in χT due the population of a less magnetic state. For $\Delta E = 1000 \text{ cm}^{-1}$, there is a TIP behavior when $\|\mathbf{M}_{12}\|^2 \neq 0$. For $\Delta E = 200 \text{ cm}^{-1}$, the saturation is not reached at room temperature, and χT is in a regime between Curie-type and TIP.

room temperature is not a good indicator of the oxidation state and presents a large window around the μ_J values.

Fig. 2 Effective moments μ_{eff} (μ_B) of aqueous actinide cations at 298 K. Filled symbols: in perchlorate acid solution, with the Evans method, from ref. [20]. empty symbols: in $[\text{An}(\text{H}_2\text{O})_9](\text{CF}_3\text{SO}_3)_3$ crystals, with SQUID, from ref. [21]. Dashed line: Russell-Saunders coupling scheme from Eq. 15.

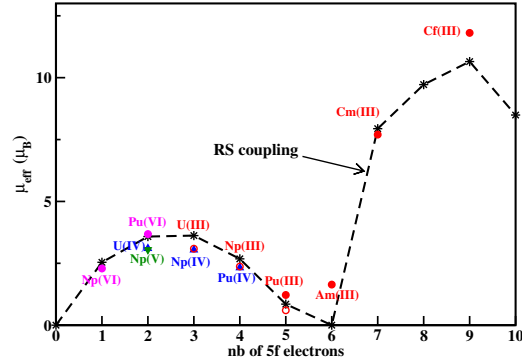


Table 1 Molar magnetic susceptibility χ ($10^{-8} \text{ m}^3 \text{ mol}^{-1}$) for aquo actinide complexes, according to Russell-Saunders coupling scheme (RSC), measured by Evans method in solution in perchloric media (exp), and deduced from SO-CASPT2 calculations (calc), from refs. [22, 23].

An	f^n	$2S+1 L_J$	RSC	exp ^a	calc ^b
U(IV)	2	3H_4	6.75	5.07 (± 0.18)	5.63
Np(IV)	3	$^4I_{9/2}$	6.90	4.86 (± 0.08)	4.89
Pu(IV)	4	5I_4	3.80	2.84 (± 0.07)	2.91
Pu(III)	5	$^6H_{5/2}$	0.38	0.79 (± 0.02)	0.75
Am(III)	6	7F_0	0	1.41 (± 0.04)	0.86
Cm(III)	7	$^8S_{7/2}$	33.3	31.3 (± 0.8)	31.6

^a corrected from radioactivity. ^bSO-CASPT2 on the $[\text{An}(\text{H}_2\text{O})_9]^{n+}$ complex, with a geometry optimized by DFT, the An-O distance fixed at the experimental EXAFS one.

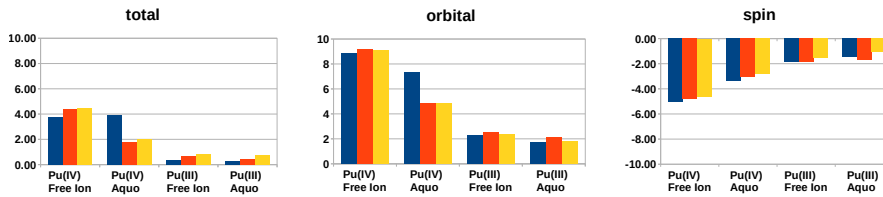


Fig. 3 Magnetic susceptibility and orbital and spin contributions ($10^{-8} \text{ m}^3 \text{ mol}^{-1}$) for Pu(IV) and Pu(III) free ions and aquo $[\text{An}(\text{H}_2\text{O})_9]^{n+}$ complexes. From CASPT2. Blue: LS; orange: ground J-manifold; yellow: all states. The spin contribution is negative.

The magnetic susceptibility of aquo actinide complexes deduced from NMR measurement with the Evans method [15] in perchlorate media [20] and measured

3 Model Hamiltonians

Within crystal-field theory, the Hamiltonian describing the f electrons may be written as

$$\hat{\mathcal{H}}^{CF} = \sum_{i=1}^N \left[\hat{T}_i - \frac{Z^* e^2}{4\pi\epsilon_0 r_i} \right] + \sum_{i<j} \frac{e^2}{4\pi\epsilon_0 r_{ij}} + \sum_{i=1}^N \zeta \hat{\mathbf{l}}_i \cdot \hat{\mathbf{s}}_i + \sum_{i=1}^N \hat{v}^{CF}(\mathbf{r}_i) \quad (16)$$

with the scalar relativistic kinetic term, the attraction of the electrons by the screened charge of the metal nucleus Z^* , the electron-electron repulsion, the spin-orbit operator, and the crystal-field operator, respectively. \mathbf{r}_i is the nucleus-electron position vector and r_{ij} the electron-electron distance. The sum runs over the N f electrons of the valence shell. This Hamiltonian acts in the whole $5f^N$ configuration space. The parameters are the three Slater-Condon parameters for electron-electron repulsion F^2 , F^4 and F^6 [29], the effective one-electron spin-orbit coupling parameter ζ and the crystal-field parameters defined at the orbital level (see Section 3.1). They can be fitted to experimental data (as for example using the code CONDON, [30]) or deduced from ab initio calculations, (AILFT, [31]). This full crystal-field Hamiltonian can be used to build model Hamiltonians built in a smaller active space, with effective parameters [30, 32, 33].

Model parameters can be evaluated from ab initio calculations [34], and model Hamiltonians enable experiment and theory to meet easily, by comparing the parameters fitted to experimental data and evaluated from computational quantum chemistry. Quantum chemistry provides the eigenstates of the zero-field Hamiltonian $\hat{\mathcal{H}}^0$; a subspace spans the model space. In the case of very few parameters, it might be sufficient to fit them to reproduce the ab initio energies. Otherwise, the information born by the wave-functions is necessary; for that, one needs to make a one-to-one connection between the ab initio and model states. If quite straightforward for spin-only manifolds of transition metal complexes modeled by Spin Hamiltonians, in the case of actinide complexes where the orbital component is dominant, this connection is not as simple. It is performed by diagonalizing the representation matrix of $\hat{\mathbf{M}}_Z$ in the model space, which provides the $|S, M_S\rangle$ or $|J, M_J\rangle$ kets. The phase factors between the states is further determined such that the superdiagonal of the representation matrix of \hat{M}_X which is real [35, 36]. Once the connection is performed, the representation matrix of the zero-field Hamiltonian is written in this basis set and compared to the representation of the model Hamiltonian in the model space.

3.1 Crystal-field Hamiltonian

In lanthanide complexes, the Russell-Saunders coupling scheme applies well, the J-mixing of the ground term of the free ion $^{2S+1}L_J$ with excited states is negligible. In a complex, the splitting of the ground J manifold is of some hundreds of cm^{-1} , due to the small interaction of the $4f$ orbitals with the ligands. The splitting of the many-electron term results from the splitting of the $4f$ orbitals, namely a one-electron interaction. In the free ion, the components of the J-manifold are built according to the Clebsch-Gordan coupling scheme

$$|J, M_J\rangle = \sum_{M_L=M_L+M_S} \langle LM_L SM_S | J, M_J \rangle |L, M_L; S, M_S\rangle \quad (17)$$

Since the splitting between the $4f$ orbitals is much smaller than the electron-electron repulsion, the composition of the states is kept the same in the presence of the ligands, as revealed by the analysis of the SO-CASSCF wave-functions [37].

The splitting of the 4f orbitals can be described by crystal-field theory. It has been developed as a pure electrostatic interaction, but the parameters are phenomenological, and includes any other interaction. Assuming that all the 4f orbitals have the same spatial expansion, the crystal-field operator is expressed by the tensor operators \hat{O}_q^k acting in either the l (one-electron), L (spin-free) or J (spin-orbit) manifolds.

$$\hat{V}^{CF}(X) = \sum_{k=2,4,6} \alpha_X^k \sum_{q=-k}^k B_q^k \hat{O}_q^k(X) \quad (18)$$

where $X = l, L, J$ according to the considered manifold [38, 39]. The $\alpha_X^k = \langle X || \alpha^k || X \rangle$ are the reduced matrix elements of 2nd, 4th and 6th orders respectively. The α_l^k are determined by N , the α_L^k by N and L , and the α_J^k by N, L and J . These reduced matrix elements are tabulated for the ground state of each lanthanide ion [40]. The convention of Wybourne is used throughout this work [41, 42]. The crystal-field parameters B_q^k can be calculated from CAS based wave-functions, either at the orbital level ($X = l$) using the ab initio ligand-field theory (AILFT) [43], or from many-electron states, without or with spin-orbit coupling ($X = L$ or J) [36]. The crystal-field parameters calculated at those different levels are very similar, confirming that the splitting of the ground J-manifold can be analyzed at the orbital level [44]. In f elements, there are in general 27 parameters; this number is reduced by symmetry. The crystal-field parameters depend on the orientation of the molecule in the Cartesian frame and it is convenient for the sake of comparison between different complexes and for complexes without symmetry to introduce the crystal-field strength parameter [45]

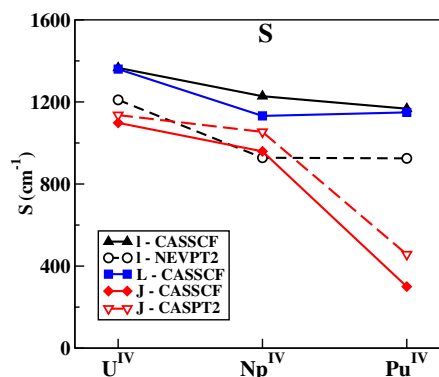
$$S = \left[\frac{1}{3} \sum_{k=2,4,6} \frac{1}{2k+1} \sum_{q=-k}^k |B_q^k|^2 \right]^{1/2} \quad (19)$$

which is rotational invariant. The parameter S allows to evaluate the strength of the ligand field with only one parameter and gives an idea of the overall splitting of the ground J-multiplet.

In actinide complexes, by comparing to lanthanide complexes, i) the interaction of the 5f orbitals with the ligands is more important because of a larger radial expansion and a less effective screening by the occupied 6s6p shell ii) the electron-electron interaction in the 5f shell is smaller due to the radial node of the 5f orbitals and larger spatial extension iii) the J-mixing is more important due to large spin-orbit coupling, and the states should be analyzed within the intermediate coupling scheme. Anyhow, the $2J + 1$ lowest states are well separated from the others and can be assigned to

arise from the ground J-manifold. The analysis of the wave-functions with spin-orbit reveals that all LS components contribute, but the weights do not follow those of the Clebsch-Gordan scheme of Eq. 17: the lowest 5f orbitals participate more to the ground state than the highest. In this case, the crystal-field parameters can be defined as in Eq. 18 using the same techniques as for lanthanide complexes. The results for the $[\text{An}^{\text{IV}}(\text{DPA})_3]^{2-}$ ^(b) series are shown in Fig. 4. The U(IV) ($5f^2$) and Np(IV) ($5f^3$) reveal a small reduction (about 10-15 %) of the crystal-field strength parameter S from orbital ($l = 3$) to many-electron including spin-orbit (J) levels. For the Pu(IV) complex ($5f^4$), S is divided by a factor of 3, pointing out again the strong J-mixing in Pu complexes, as already noted in aquo complexes (cf Section 2.1). For the two former, the crystal-field parameters deduced from the J-manifold follow the orbital level. But, for the Pu(IV) complex, little can be anticipated from the orbital level to rationalize the many-electron levels with spin-orbit. This is confirmed by studies based on the complete crystal-field Hamiltonian of Eq. 16 in the full $5f^N$ configuration as compared to a limited one restricted to the ground J-multiplet [46]. Actually, the crystal-field parameters deduced from a J-multiplet provide effective crystal-field parameters whose physical meaning incorporates many-electron effects and J-mixing and differ from one J-multiplet to the other. The many-electron crystal-field parameters, since they effectively account for all interactions, are suitable to reproduce the magnetic properties which arise only from the ground J-manifold. On the other hand, the orbital crystal-field parameters are more appropriate for the modeling of optical spectra, since they are unequivocal. It is then possible to calculate the whole spectrum using the Slater-Condon and spin-orbit parameters.

Fig. 4 Crystal-field strength parameter S in the $[\text{An}^{\text{IV}}(\text{DPA})_3]^{2-}$ series calculated with different CAS based methods, for different manifolds $X = l, L, J$.



^(b) DPA = pyridine-2,6-dicarboxylic acid

Magnetic properties are often described by Spin Hamiltonians, where all operators are expressed using spin operators. For transition metal complexes, they are very close to the true spin operators, but in actinide complexes, due to the large orbital contribution, the spin is by far not a good quantum number. In this case, the spin is called a pseudo-spin \mathcal{S} , to avoid any confusion with a real spin. Its value is taken to fit the size of the model space $2\mathcal{S} + 1$ and the model states are expressed in terms of the $|\mathcal{S}, \mathcal{M}\rangle$ [40, 47, 48].

The simplest Spin Hamiltonian is for doublet states, described by a pseudo-spin $S = 1/2$. For Kramers ions, the doublet is degenerate in zero-field, and only the Zeeman interaction is modeled by the g-tensor

where $\hat{\mathbf{S}}$ is the pseudo-spin operator. A Kramers doublet is described by two Kramers partners related by time-reversal symmetry

where $\hat{\Theta}$ is the time-inversion operator. There is a multitude of choice for the $\Psi, \bar{\Psi}$ couple. The g-matrix is calculated as [40, 49]

with $u = x, y, z$. This matrix is in general neither symmetrical, nor a tensor, but its square $G = g^\dagger \cdot g$ is. G provides the principal axes frame of the g -tensor and the squared g -factors. Their signs are consequently undetermined. In the principal axes frame (X, Y, Z) of the g -tensor, the magnetic moment operator takes the canonical form

The orbital and spin contributions to the g-factors are calculated as

$$\begin{aligned}
g_X^L &= 2 \operatorname{Re} \langle \bar{\Psi} | \hat{L}_X | \Psi \rangle ; g_X^S = 4 \operatorname{Re} \langle \bar{\Psi} | \hat{S}_X | \Psi \rangle ; g_X = g_X^L + g_X^S \\
g_Y^L &= 2 \operatorname{Im} \langle \bar{\Psi} | \hat{L}_Y | \Psi \rangle ; g_Y^S = 4 \operatorname{Im} \langle \bar{\Psi} | \hat{S}_Y | \Psi \rangle ; g_Y = g_Y^L + g_Y^S \\
g_Z^L &= 2 \langle \Psi | \hat{L}_Z | \Psi \rangle ; g_Z^S = 4 \langle \Psi | \hat{S}_Z | \Psi \rangle ; g_Z = g_Z^L + g_Z^S
\end{aligned} \tag{24}$$

In other words, when the magnetic field is applied in one principal direction U of g , the magnetic moment for this Kramers doublet is

$$M_U = \pm \frac{1}{2} g_U \tag{25}$$

The anisotropy of g is due to orbital contributions [48], and is important in actinide complexes. g -factors can be negative. If $|g_X| \approx |g_Y| \ll |g_Z|$, the magnetization of the doublet is prolate, if $|g_Z| \ll |g_X| \approx |g_Y|$, it is oblate.

Non-Kramers doublet

States of symmetrical non-Kramers ions can be two-fold, due to spatial symmetry. The two states $|1\rangle$ and $|2\rangle$ are not related by time-reversal symmetry and might split by an energy gap Δ [50]. According to Eq. A2 of Appendix, the magnetic moment of a non-degenerate state vanishes. In other words, $\langle 1 | \hat{M}_u | 1 \rangle = \langle 2 | \hat{M}_u | 2 \rangle = 0$, but $|1\rangle$ and $|2\rangle$ might be coupled by the Zeeman Hamiltonian, for example in direction X , $\langle 1 | \hat{M}_X | 2 \rangle \neq 0$. The spin Hamiltonian takes the form in the $|1\rangle, |2\rangle$ basis set

$$\hat{\mathcal{H}}^S = \Delta \hat{S}_Z + \mu_B g B_X \hat{S}_X \tag{26}$$

There is only one non-zero g -factor. The magnetic response in directions other than X is due to second-order Zeeman interaction with other manifolds.

Quartet

As an example, the ground state of the octahedral $[\text{Np}^{\text{IV}}\text{Cl}_6]^{2-}$ cluster diluted in Cs_2ZrCl_6 crystal is a quartet. The ground state is a quartet $F_{3/2u}$ (using Mulliken's notation) [35] and is described by a $\mathcal{S} = 3/2$ pseudo-spin. There is no zero-field term, the Zeeman term is isotropic and needs a cubic term. In the principal axes frame, the spin Hamiltonian takes the form [51]

$$\hat{\mathcal{H}}^S = \mu_B g \hat{\mathbf{S}} \cdot \mathbf{B} + \mu_B g' \left(B_X \hat{S}_X^3 + B_Y \hat{S}_Y^3 + B_Z \hat{S}_Z^3 \right) \tag{27}$$

The two scalar g and g' parameters were deduced from EPR measurements as $g = -0.516$ and $g' = 0.882$. When an external magnetic field is applied, a pure spin quartet splits into four uniformly distributed components, with energies $\mu_B g_e M_S$.

When the complex is distorted, the quartet splits into two Kramers doublets. Supplementary terms should be added to Eq. 27. It becomes then more intuitive to model the quartet by two interacting doublets, each with a g-tensor coupled by second-order Zeeman interaction [52].

4.1 Spinor scheme

In the free linear cations, without spin-orbit coupling, the ϕ are lower in energy than the δ because more distant from the oxo/nitride groups, and this reduces the electrostatic repulsion. In the presence of an equatorial ligand, the δ are often lower than the ϕ , because the latter are now closer from the equatorial ligands and this is unfavorable on a electrostatic point of view, and involved in σ anti-bonding with the orbitals of the ligands, while the δ have π interactions. The δ and ϕ orbitals have m_l values of ± 2 and ± 3 , respectively. When the degeneracy is lifted, the angular moment is quenched, but partially recovered by coupling the two orbitals: the closer the two orbitals, the larger the angular moment. As shown in Figure 5, the $e_{3/2}$ and $e_{5/2}$ spinors are very close in energy, and one or the other one can be the ground spinor, according to the nature of the axial and equatorial ligands. The former is a pure $\delta_{3/2}$ while the composition of the latter is a mixing between the $\delta_{5/2}$ and $\phi_{5/2}$.

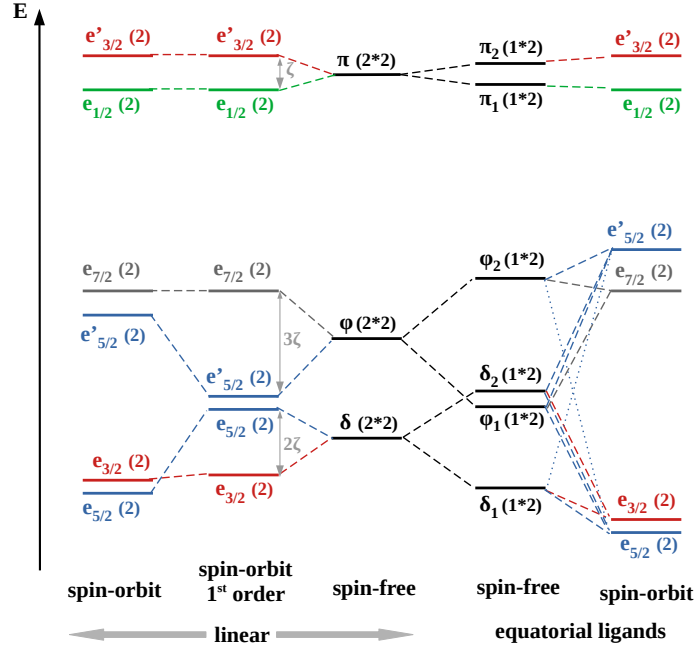


Fig. 5 5f spinors for $[\text{AnO}_2]$, $[\text{AnO}]$, $[\text{AnN}_2]$ or $[\text{AnN}]$ units, linear (left) or with equatorial ligands (right). The degeneracy of the states in given in parentheses.

The axial ligands determines the δ - ϕ splitting, and the nature and the symmetry of the equatorial ligands the splitting of the δ and/or ϕ orbitals.

4.2 g-factors

Spin-orbitals are given in terms of spherical harmonics in Table A1 in Appendix and the representation matrix of the spin-orbit operator $\hat{h}^{SO} = \zeta \hat{\mathbf{l}} \cdot \hat{\mathbf{s}}$ in the basis of the spin-orbitals in Table A3 in Appendix. The crystal-field operator \hat{h}^{CF} is diagonal, and the representation matrix of $\hat{h} = \hat{h}^{CF} + \hat{h}^{SO}$ in the δ and ϕ spin-orbitals basis is

$$\begin{array}{c|cccc}
 \hat{h} & |\delta_1\rangle & |\delta_2\rangle & |\bar{\phi}_1\rangle & |\bar{\phi}_2\rangle \\
 \hline
 \langle \delta_1 | & \varepsilon_{\delta 1} & i\zeta & -\frac{\sqrt{3}\zeta}{2\sqrt{2}} & -i\frac{\sqrt{3}\zeta}{2\sqrt{2}} \\
 \langle \delta_2 | & -i\zeta & \varepsilon_{\delta 2} & i\frac{\sqrt{3}\zeta}{2\sqrt{2}} & -\frac{\sqrt{3}\zeta}{2\sqrt{2}} \\
 \langle \bar{\phi}_1 | & -\frac{\sqrt{3}\zeta}{2\sqrt{2}} & -i\frac{\sqrt{3}\zeta}{2\sqrt{2}} & \varepsilon_{\phi 1} & -i\frac{3\zeta}{2} \\
 \langle \bar{\phi}_2 | & i\frac{\sqrt{3}\zeta}{2\sqrt{2}} & -\frac{\sqrt{3}\zeta}{2\sqrt{2}} & i\frac{3\zeta}{2} & \varepsilon_{\phi 2}
 \end{array} \quad (28)$$

$$\begin{aligned} |\psi\rangle &= a|\delta_1\rangle + b|\delta_2\rangle + c|\bar{\phi}_1\rangle + d|\bar{\phi}_2\rangle \\ |\bar{\psi}\rangle &= \hat{\Theta}|\psi\rangle = a^*|\bar{\delta}_1\rangle + b^*|\bar{\delta}_2\rangle - c^*|\phi_1\rangle - d^*|\phi_2\rangle \end{aligned} \quad (29)$$
$$\begin{aligned}
g_{\parallel}^L &= 2 \langle \psi | \hat{l}_z | \psi \rangle = 8\text{Im}(a^*b) + 12\text{Im}(cd^*) \\
g_{\parallel}^S &= 4 \langle \bar{\psi} | \hat{s}_x | \psi \rangle = 2 \left(|a|^2 + |b|^2 - |c|^2 - |d|^2 \right) \\
g_X^L &= 2\text{Re} \langle \bar{\psi} | \hat{l}_x | \psi \rangle = 2\sqrt{6}\text{Im}(bd - ac) \\
g_Y^L &= 2\text{Im} \langle \bar{\psi} | \hat{l}_y | \psi \rangle = -2\sqrt{6}\text{Re}(ad + bc)
\end{aligned} \tag{30}$$

$$g_{\parallel} = g_{\parallel}^L + g_{\parallel}^S$$

$$g_{\perp} = g_{\perp}^L + g_{\perp}^S$$

- $\varepsilon_{\delta 2} - \varepsilon_{\delta 1}$ is very large. $|\psi\rangle = |\delta_1\rangle$ is a pure spin state. $g_{\parallel}^S = g_{\perp}^S = 2$, $g_{\parallel}^L = g_{\perp}^L = 0$, \mathbf{g} is isotropic, as expected.
- $\varepsilon_{\delta 2} - \varepsilon_{\delta 1} = 0$.

- $|\psi\rangle = \frac{1}{\sqrt{2}}(|\delta_1\rangle + i|\delta_2\rangle)$ corresponds to the $\delta_{5/2}$ spinor. $g_{\parallel}^L = 4$, $g_{\parallel}^S = 2$, $g_{\parallel} = 6$, $g_{\perp}^L = g_{\perp}^S = g_{\perp} = 0$. \mathbf{g} is purely axial, with additive orbital and spin contributions.
- $|\psi\rangle = \frac{1}{\sqrt{2}}(|\delta_1\rangle - i|\delta_2\rangle)$ corresponds to the $\delta_{3/2}$ spinor. $g_{\parallel}^L = -4$, $g_{\parallel}^S = 2$, $g_{\parallel} = -2$. $g_{\perp}^L = g_{\perp}^S = g_{\perp} = 0$. \mathbf{g} is purely axial, with opposite orbital and spin contributions, leading to a negative \mathbf{g} -factor.

It shows how the energy gap between the two δ orbitals tunes the g-tensor from either isotropic to axial with positive or negative values, with all intermediate situations.

The $[\text{NpO}_2]^{2+}$ and $[\text{UN}]^{2+}$ units were probed with different equatorial ligands and described by SO-CAS based methods, as summarized in Table 2. In the $[\text{NpO}_2(\text{NO}_3)_3]^-$ complex, with a ternary symmetry, the two ϕ orbitals are largely split by 5000 cm^{-1} and the ground state is 75% on the ϕ orbitals. A combined analysis using EPR and absorption in a magnetic field allowed to determine the energies and g-factors of the excited states, and the sign of the longitudinal components g_{\parallel} . All those values are well reproduced by SO-CASPT2 and by Eqs. 31 [54]. In the $[\text{NpO}_2\text{Cl}_4]^{2-}$ complex, with a four-fold symmetry, the splitting of the δ is about 1000 cm^{-1} . The ground Kramers doublet in this case is 92 % on the δ orbitals in good accordance with the EPR data. It was needed to introduce the coupling with the π orbitals to approach the experimental values. In the $[\text{NpO}_2(\text{DPA})_2]^{2-}$ complex, the symmetry of the equatorial ligands is approximately ternary. The magnetic susceptibility measured using Evans method in solution, and by SQUID in the solid state are different. This is due to two Li^+ cations positioned between two DPA^{2-} ligands [52]. The calculations revealed that the composition of the ground Kramers doublet is strongly affected, 62 % δ in solution, 67 % ϕ in solid state. In this case, a large active space was necessary to get the correct g-factors. The ground Kramers doublet of the $[\text{UN}]^{2+}$ unit is similar to $[\text{NpO}_2]^{2+}$, namely close to a $\phi_{5/2}$ spinor. The π and σ orbitals are lower (5000 and 6000 cm^{-1}) than in the $[\text{NpO}_2]^{2+}$ unit (20000 and 30000 cm^{-1}) since there is only one triple bond. While coordinated by the equatorial Tren^(c) ligand, the $e_{3/2}$ and $e_{5/2}$ are extremely close and one or the other one can be the ground state, according to the terminal ligands as ethercrowns. The $e_{3/2}$ doublet is EPR silent. The energy gap is sufficiently small that the $e_{5/2}$ is detected, even when excited. The nature of the ground doublet is provided by magnetometry and confirmed by SO-CASSCF [55]. The similar complex with the $[\text{UO}]^{3+}$ unit is EPR silent, denoting a $e_{3/2}$ ground state.

To conclude, according to the nature of the equatorial ligand, the magnetization of the ground Kramers doublet can be almost axial $g_{\perp} \approx 0$, spherical $g_{\parallel} \approx g_{\perp}$ and even slightly oblate. Those properties are finely tuned by the energies of the four δ and ϕ orbitals $\varepsilon_{\delta 1}$, $\varepsilon_{\delta 2}$, $\varepsilon_{\phi 1}$ and $\varepsilon_{\phi 2}$.

4.3 Natural spin orbitals

The g-factor of a given Kramers doublet represents the magnetic moment in the corresponding direction as expressed in Eq. 25, with both orbital and spin contributions. The spin magnetization depends on the direction u of the magnetic field due to spin-orbit coupling and is related to the spin g-factor according to

$$\int m_u^S(\mathbf{r}) d\mathbf{r} = \frac{1}{4} \mu_B g_u^S \quad (32)$$

^(c) Tren= tris(2-aminoethyl)amine

The Natural Spin Orbitals (NSOs) are the natural orbitals issued from the spin magnetization for a given direction of the external magnetic field [54, 60, 61]. In direction z , $|\psi\rangle$ and $|\bar{\psi}\rangle$ of Eq. 29 are eigenvectors of the \hat{s}_z operator, and the spin magnetization density can be calculated as

$$\begin{aligned} m_z^S(\mathbf{r}) &= \mu_B \psi^\dagger(\mathbf{r}) \hat{s}_z \psi(\mathbf{r}) \\ &= \frac{\mu_B}{2} \left(|a|^2 |\delta_1(\mathbf{r})|^2 + |b|^2 |\delta_2(\mathbf{r})|^2 - |c|^2 |\phi_1(\mathbf{r})|^2 - |d|^2 |\phi_2(\mathbf{r})|^2 \right) \end{aligned} \quad (33)$$

δ_1 , δ_2 , ϕ_1 and ϕ_2 orbitals are the NSOs in z direction, with respective populations $|a|^2$, $|b|^2$, $-|c|^2$ and $-|d|^2$. As expected, the two orbitals with α spin in $|\psi\rangle$ contribute positively, the two with β spin, negatively. The NSOs in the perpendicular direction are less intuitive. The eigenvectors of \hat{s}_x are $|\psi_x\rangle = \frac{1}{\sqrt{2}} (|\psi\rangle + |\bar{\psi}\rangle)$ and $|\bar{\psi}_x\rangle = \frac{1}{\sqrt{2}} (|\psi\rangle - |\bar{\psi}\rangle)$. Written as spinors,

$$\begin{aligned} |\psi_x\rangle &= \frac{1}{\sqrt{2}} \begin{pmatrix} a\delta_1 + b\delta_2 - c^*\phi_1 - d^*\phi_2 \\ a^*\delta_1 + b^*\delta_2 + c\phi_1 + d\phi_2 \end{pmatrix} \\ \hat{s}_x |\psi_x\rangle &= \frac{1}{\sqrt{2}} \begin{pmatrix} a^*\delta_1 + b^*\delta_2 + c\phi_1 + d\phi_2 \\ a\delta_1 + b\delta_2 - c^*\phi_1 - d^*\phi_2 \end{pmatrix} \end{aligned} \quad (34)$$

The spin magnetization in direction x is expressed as

$$\begin{aligned} m_x^S(\mathbf{r}) &= \mu_B \psi_x^\dagger(\mathbf{r}) \hat{s}_x \psi_x(\mathbf{r}) \\ &= \frac{\mu_B}{2} \left[\text{Re}(a^2) |\delta_1(\mathbf{r})|^2 + \text{Re}(b^2) |\delta_2(\mathbf{r})|^2 \right. \\ &\quad \left. - \text{Re}(c^2) |\phi_1(\mathbf{r})|^2 - \text{Re}(d^2) |\phi_2(\mathbf{r})|^2 \right] \end{aligned} \quad (35)$$

In this case, the population of each NSO may be either positive or negative since a , b , c and d are complex. We let as an exercise to the reader to demonstrate that the same spin magnetization is obtained in direction y : $m_y(\mathbf{r}) = \psi_y^\dagger(\mathbf{r}) \hat{s}_y \psi_y(\mathbf{r}) = m_x(\mathbf{r})$ with $|\psi_y\rangle = \frac{1}{\sqrt{2}} (|\psi\rangle + i|\bar{\psi}\rangle)$.

Let us consider again the cases mentioned above.

- For the pure spin state $|\psi\rangle = |\delta_1\rangle$, $m(\mathbf{r}) = \frac{\mu_B}{2} |\delta_1(\mathbf{r})|^2$ in all directions.
- The two $\delta_{5/2}$ and $\delta_{3/2}$ spinors with $a = 1/\sqrt{2}$, $b = \pm i/\sqrt{2}$, $c = d = 0$ lead to the same spin densities

$$\begin{aligned} m_z^S(\mathbf{r}) &= \frac{1}{4} \left(|\delta_1(\mathbf{r})|^2 + |\delta_2(\mathbf{r})|^2 \right) \\ m_\perp^S(\mathbf{r}) &= \frac{1}{4} \left(|\delta_1(\mathbf{r})|^2 - |\delta_2(\mathbf{r})|^2 \right) \end{aligned} \quad (36)$$

As expected from the spin g-factors, the spin magnetization density is highly anisotropic: along z , it shows a cylinder symmetry while in the perpendicular direction, even summing up to zero, the density is locally non vanishing, with alternation of positive and negative regions.

where a and b are real with $a^2 + b^2 = 1$. They depend on Δ/ζ , the ratio between one of the crystal-field parameters and the spin-orbit coupling constant. The g-factors are calculated with Eqs. 22 [67]: they are isotropic $g_x = g_y = g_z = g$

$$\begin{aligned} g &= 2a^2 - \frac{8}{\sqrt{3}}ab \\ g^L &= -\frac{8}{\sqrt{3}}ab + \frac{2}{3}b^2 \\ g^S &= 2a^2 - \frac{2}{3}b^2 \end{aligned} \quad (38)$$

The orbital contribution arises from the coupling between a_{2u} and t_{1u} manifolds (ab term) and from the zeroth-order contribution of the t_{2u} manifold. The spin contribution has some negative contribution from the t_{2u} manifold. As shown in Fig. 7a, b varies from $2/\sqrt{7} \approx 0.75$ for the free-ion limit ($\Delta = 0$) to 0 for the spin-only limit ($\zeta = 0$). At the free-ion limit, g is negative, due to the large negative orbital contribution and ends up to 2 at the spin-only limit, where g^L vanishes.

The g-factors calculated with SO-CASPT2 in a series of $5f^1$ complexes compare well to experimental data [67, 68] as represented in Fig. 7a. In all cases, $x = \Delta/\zeta$ lies between 1 and 2, with respective ϕ_{a2u}/ϕ_{t2u} weights 57/43 ($x = 1$) and 70/30 ($x = 2$). Since the crystal-field and spin-orbit interactions are of the same order of magnitude, we are close to the free-ion limit, g is negative as confirmed by experiment and the spinor with the unpaired electron is better described by the $m_j = \pm 5/2$ component of the ${}^2F_{5/2}$ term of the free ion than by a spin-only state. The NSOs were studied in references [68, 61].

5.2 $5f^N$ octahedral complexes

The SQUID susceptibility of the $5f^2$ octahedral $[\text{U}^{\text{IV}}\text{F}_6]^{2-}$ complex reveals a TIP behavior with an inflection in the $\chi T = f(T)$ curve. The magnetic moments were determined by X-ray magnetic circular dichroism (XMCD) spectroscopy [69] which allows to deconvolute the spin and orbital contributions: $M^L = 0.47\mu_B$, $M^S = -0.41\mu_B$ and $M = M^L + M^S = 0.060\mu_B$ with a field of 17 T and a temperature of 4 K [70]. NEVPT2 calculations show that without spin-orbit, the ${}^3T_{1g}$ ground state is a mixing of $a_{2u}t_{2u}$ and t_{2u}^2 configurations. With spin-orbit, the ground non-degenerate A_{1g} state is issued by 90% from the spin triplet ${}^3T_{1g}$ with 10% coupling with an excited spin singlet ${}^1A_{1g}$. Within a j-j coupling perspective, the closed-shell $e_{5/2u}^2$ configuration leads to a A_{1g} ground state; since the spinor $e_{5/2u}$ of Eq. 37 is a mixing of α and β spin-orbitals, this leads to spin singlet determinants as for example $|\delta_2\bar{\delta}_2|$, $|\delta_1\bar{\delta}_1|$, as well as spin triplet ones as $|\delta_{1,2}\pi_{1,2}|$ and $|\delta_{1,2}\phi_{1,2}|$. The composition of this ground state is halfway between the j-j and LS coupling schemes, and difficult to anticipate without numerical treatment. The SO-NEVPT2 calculation finds a pure TIP type susceptibility due to the coupling of the non-magnetic ground state with a

The ground state of the $5f^3 [\text{NpCl}_6]^{2-}$ cluster diluted in Cs_2ZrCl_6 crystal is a $F_{3/2u}$ state. It is highly multi-configurational. It could be noticed that the j-j coupling scheme leads to the $e_{5/2u}^2 f_{3/2u}$ configuration, of $F_{3/2u}$ symmetry. Within a LS coupling scheme perspective, the spin-orbit couples the two spin-free 4A and 4T states separated by 2500 cm^{-1} with important contributions on spin doublet states.

The spinor scheme in tetrahedral symmetry is given in Fig. 6c. The a_1 orbital is σ anti-bonding with the orbitals of the ligands: the orbitals follows a $t_1 < t_2 \ll a_1$ scheme leading to a ground $f_{3/2}$ spinor, of dominant t_1 nature. The $5f^2 \text{U}^{\text{IV}}(\text{NSiMe}_3)_4]^-$ complex has a pseudo-tetrahedral symmetry. The ground state is a non-Kramers doublet E compatible with an open-shell $f_{3/2}^2$ spinor configuration, issued from the t_1^2 orbital configuration. SO-CASSCF reveals a small splitting by 11 cm^{-1} of the ground doublet, and reproduces well both the magnetization and susceptibility curves. The complexes $\text{U}^{\text{IV}}(\text{O})(\text{NSiMe}_3)_3]^-$ has a trigonal bipyramidal symmetry with the $[\text{U}^{\text{IV}}\text{O}]^{2+}$ unit discussed in Section 4.1, approaching a trigonal symmetry. The ground non-Kramers doublet splits by 39 cm^{-1} according to SO-CASSCF, which is a slight overestimation of the experimental gap of 5 cm^{-1} [64], leading to different magnetization curves. Those curves are very sensitive to

the gap of non-Kramers doublet [73]. There is a singlet around 200 cm^{-1} and then at 1000 cm^{-1} which leads to a complex χT behavior: the ab initio curve fits well the experimental one above 50 K.

6 Sandwich complexes

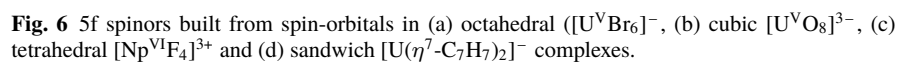
In sandwich complexes, the actinide ion is between two planar aromatic rings. We will consider the $(\eta^7\text{-C}_7\text{H}_7)^-$ and $(\eta^8\text{-C}_8\text{H}_8)^{2-} = \text{COT}^{2-}$ ligands. The staggered $[\text{An}(\eta^7\text{-C}_7\text{H}_7)_2]^{n-}$ and eclipsed $[\text{Np}(\text{COT})_2]$ structures have \mathcal{D}_{7d} and \mathcal{D}_{8h} symmetries, respectively, but can be treated as $\mathcal{D}_{\infty h}$ [74]. The spinor diagram is given in Fig. 6d. In the previous sections, the $5f$ orbitals were anti-bonding with the orbitals of the ligand. In aromatic ligands, some π molecular ligands' orbitals are occupied, other are vacant: the $5f$ are either bonding or anti-bonding. The two $(\eta^7\text{-C}_7\text{H}_7)^-$ and COT^{2-} ligands have a π occupation $a_1^2 e_1^4 e_2^4$. The highest occupied orbitals are e_2 with axial symmetry δ , the lowest unoccupied orbitals are e_3 with axial symmetry ϕ ; as a consequence for the $5f$, the strong destabilization of the δ and the stabilization of the ϕ [37, 75]. Furthermore, the ϕ and δ orbitals point in the direction of the carbon atoms of the ligands, and are electrostatically destabilized as compared to the σ and π . The lowest orbital is the σ , and the π and ϕ closely above. The ground spinor is of symmetry $e_{1/2}$, a mixing of σ and π spin-orbitals by spin-orbit coupling

$$\begin{aligned} |\psi\rangle &= a|\sigma\rangle + \frac{b}{\sqrt{2}}(i|\bar{\pi}_1\rangle + |\bar{\pi}_2\rangle) \\ |\bar{\psi}\rangle &= \hat{\Theta}|\psi\rangle = a|\bar{\sigma}\rangle + \frac{b}{\sqrt{2}}(i|\pi_1\rangle - |\pi_2\rangle) \end{aligned} \quad (39)$$

where a and b are real numbers with $a^2 + b^2 = 1$. The different components to the g-factors are calculated from Eqs. 22 [76, 75]

$$\begin{aligned} g_{\parallel}^L &= 2\langle\psi|\hat{l}_z|\psi\rangle = 2b^2 \\ g_{\parallel}^S &= 2\langle\bar{\psi}|\hat{s}_x|\psi\rangle = 2(a^2 - b^2) \\ g_{\perp}^L &= 4\text{Re}\langle\bar{\psi}|\hat{l}_x|\psi\rangle = -4\sqrt{3}ab \\ g_{\perp}^S &= 4\text{Re}\langle\bar{\psi}|\hat{s}_x|\psi\rangle = 2a^2 \\ g_{\parallel} &= 2a^2 \\ g_{\perp} &= 2a^2 - 4\sqrt{3}ab \end{aligned} \quad (40)$$

The composition of ψ depends on $x = \Delta/\zeta$ where Δ is the $\sigma - \pi$ gap and ζ the spin-orbit constant. The variation of the g-factors is shown in Fig. 7b. Since the σ orbital is non-degenerate, for $\zeta = 0$, one obtains isotropic spin-only g-factors $g_{\parallel} = g_{\perp} = g_{\parallel}^S = g_{\perp}^S = 2$. The g-tensor is more and more anisotropic with increasing



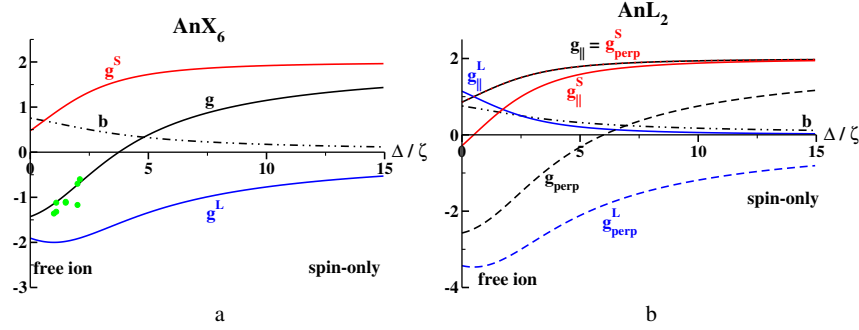


Fig. 7 Variation of g-factors with orbital and spin components, and composition of the ground Kramers doublet with Δ/ζ . g (black), g^L (blue), g^S (red) and b (dash-dotted) (a) $5f^1$ octahedral complexes, from Eqs. 37 and 38, $\Delta = \varepsilon_{t2u} - \varepsilon_{a2u}$. Green circles show the SO-CASPT2 results for $[\text{AnX}_6]^{n-}$ complexes [67]. (b) $5f^1$ sandwich complexes, \parallel (plain), \perp (dashed) from Eqs. 39 and 40, $\Delta = \varepsilon_\pi - \varepsilon_\sigma$.

mixing, the orbital contribution becomes the largest, g_\perp negative. At the free-ion limit, $x = 0$, g_\perp^S is negative as well, and one gets the $m_j = \pm 1/2$ component of the $j = 5/2$ multiplet.

The g-factors of the ground Kramers doublet of the $5f^1 [\text{U}^\text{V}(\eta^7\text{-C}_7\text{H}_7)_2]^-$ complex were measured by EPR ($g_\parallel = 1.24$ and $g_\perp = 2.37$) [76] and calculated with SO-CASPT2 [77]. The g-factors are similar to the $[\text{Ce}^\text{III}(\text{COT})_2]^-$ complex (see Table 3). The two complexes are close to the free-ion limit with $x = 0.74$ and 2, for the lanthanide and actinide complexes, respectively. In the latter, the crystal-field gap is larger due to a larger covalency but the spin-orbit constant as well, and this leads to similar ground Kramers doublet. In the $[\text{U}^\text{V}(\eta^7\text{-C}_7\text{H}_7)_2]^-$ complex, it is necessary to increase the active space to approach the experimental values, in order to better describe the covalent effects. The susceptibility, measured by SQUID, shows a TIP behavior above 50 K, compatible with those g-factors (The curves are not compared) [78]. The first excited state is the $\phi_{5/2}$ at 3200 cm^{-1} . The K-edge X-ray absorption spectroscopy reveals the implication of δ bonding in both the ground state and excited states.

Table 3 g-factors in $4f^1$ and $5f^1$ sandwich complexes.

	$[\text{Ce}^\text{III}(\text{COT})_2]^-^a$			$[\text{U}^\text{V}(\eta^7\text{-C}_7\text{H}_7)_2]^-^b$			
	CAS(1,7)PT2	mod ^c	exp	CAS(1,7)SCF	CAS(9,16)PT2	mod ^d	exp
g_\parallel	1.06	1.07	1.123	1.41	1.38	1.40	1.24
g_\parallel^L		0.93		0.55	0.60	0.60	
g_\parallel^S		0.14		0.84	0.78	0.80	
g_\perp	-2.33	-2.39	2.272	-1.57	2.23	-1.77	2.37
g_\perp^L		-3.46		-3.00	-3.60	-3.17	
g_\perp^S		1.07		1.43	1.39	1.40	

^a from ref. [75]. ^b from ref. [77]. ^c from Eqs. 40 with $\alpha^2 = 0.534$. ^d from Eqs. 40 with $\alpha^2 = 0.7$.

Complexes with configuration $5f^4$ [$\text{Np}^{\text{III}}(\text{COT})_2$] $^-$ and [$\text{Pu}^{\text{IV}}(\text{COT})_2$] have a non-magnetic ground state with first excited states at 800 and 1700 cm^{-1} respectively, leading to a pure TIP susceptibility, as calculated with SO-CASPT2. Finally, the $5f^5$ [$\text{Pu}^{\text{III}}(\text{COT})_2$] $^-$ complex has three low-lying Kramers doublets at 80 and 300 cm^{-1} , deduced from SO-CASPT2 [87].

(e) Tp = trispyrazolylborate, Tp* = hydrotris-(3,5-dimethylpyrazolyl)borate, BPz = pyrazolborate, DIB = diimidobenzene, DEB = diethynylbenzene

Some of the complexes were probed

- by Electronic Paramagnetic Resonance (EPR)
[U(Cp^{II})₃] [93], Cp^{III}₃U^IBuNC, Cp^{III}₃UCyNC [94], [U(SiMe₂NPh₃ – tacn)],
[U(SiMe₂NPh₃ – tacn)(OPPh₃)] [95].
- using Magnetic Circular Dichroism (MCD)
[Tp^{*}UI₂], [Tp₂^{*}UI], [Tp^{*}UBn] [96], [U(SiMe₂NPh₃ – tacn)],
[U(SiMe₂NPh₃ – tacn)(OPPh₃)] [95].

Many of those complexes were described by SO-CAS based methods:

[U(Tp^{Me2})₂I], [U(Tp^{Me2})₂(bipy)] [97], [98], [U(H₂Bpz₂)₃], [U(Bp^{Me})₃], [U(Bc^{Me})₃],
[UTp₃], [99], Cp^{III}₃U^IBuNC, Cp^{III}₃UCyNC [94], [UTp₃], [L₂U(H₂O)₅][I]₃L₂ [88],
[U(SiMe₂NPh₃ – tacn)], [U(SiMe₂NPh₃ – tacn)(OPPh₃)] [95], [U(BcMe)₃], [U(BpMe)₃]
[100].^(f)

g-factors determined from SO-CASSCF calculation and from crystal-field parameters fitted on susceptibility curves are compared to the EPR ones in Table 4. The accordance is in general good, at the least qualitatively. The g-factors of the ground Kramers doublet probe the composition of the ground state (see Eq. 22) : it shows that the SO-CASSCF method provides a correct wave-function for the ground state.

The χT curves probed by a SQUID in the solid state, or using the Evans method, in solution, probe many states, either populated, or not, as shown in Section 2.1. They probe at the same time the energy gaps, the magnetic moments (g-factors) of the Kramers doublets and the magnetic coupling between them. It is specially sensitive to the energy gaps for the states around room temperature, where it impacts the curvature, and for the non-populated states, which impacts the slope of the TIP. The ab initio curves are not systematically calculated and compared to the experimental ones. The accordance between ab initio and experimental is sometimes satisfactory, sometimes approximate. It is usually improved by including the dynamical correlation with CASPT2 or by including more orbitals in the active space, as for example the 6d [100].

A single-molecule magnet has super-paramagnetic behavior below a certain blocking temperature. This occurs in complexes with a strongly anisotropic ground state, as for example, a Kramers doublet with a pure axial g-tensor ($g_x = g_y = 0$). The magnetic moment is consequently $\pm \frac{1}{2} \mu_B g_z$ in one direction, and vanishes in the two other ones. The energy barrier U_{eff} for the thermally-induced reversal of this magnetic moment can be deduced from AC magnetic susceptibility. In lanthanide complexes, correlations can be found between the barrier U_{eff} and the energy of the first excited state, which is the sign of an Orbach relaxation process. But in actinide complexes, the energy gaps are much larger, as seen in Section 3.1, and there is little correlation between the measured values of U_{eff} and the energy gaps of the first excited state, as shown in Table 5, which suggests that other relaxation pathways occur in actinide complexes [89].

^(f) H₂Bpz₂[−] = dihydrobis(pyrazolyl)borate, Bp^{Me} = dihydrobis(methylpyrazolyl)borate, Bc^{Me} = dihydrobis(methylimidazolyl)borate, L = ^tBuPO(NH^tPr)₂, tacn = 1,4,7-triazacyclononane, Cp^{II} = 1,3-bis-(trimethylsilyl)cyclopentadienyl, Cp^{III} = (C₅H₃^tBu₂ – 1,3)[−]

Table 4 g-factors from EPR, crystal-field parameters fitted on the susceptibility (CF) and SO-CASSCF calculations for the ground Kramers doublet of U(III) complexes.

	Cp ^{''} ₃ U ^f BuNC ^a			[U(Cp ^{''}) ₃] ^b		[U(Bp ^{Me}) ₃] ^c		[U(Bc ^{Me}) ₃] ^c	
	CAS(3,7)	CF	exp	CAS(3,7)	exp	CAS(3,7)	exp	CAS(3,7)	exp
g_x	1.97	2.12	2.42	2.27	3.05	2.60	2.62	2.52	2.57
g_y	1.97	2.12	1.75	2.02	1.65	2.60	2.62	2.52	2.57
g_z	0.61	0.81	<0.7	0.30	< 0.5	2.08	1.76	2.18	1.03

	[U(SiMe2NPh3-tacn)] ^d				[Tp*UI2] ^e		[Tp2*UI] ^e		[Tp*UBn] ^e	
	CAS(3,7)	CAS(3,19)	CF	exp	CAS(3,7)	exp	CAS(3,7)	exp	CAS(3,7)	exp
<i>g_x</i>	3.546	4.017	2.725	3.54(5)	4.49	4.84	4.59	4.20	4.83	4.55
<i>g_y</i>	2.638	2.225	2.725	2.042(4)	1.04	0.81	1.42	1.14	1.45	1.01
<i>g_z</i>	0.802	0.795	1.679	1.66(5)	0.49	0.15	0.66	0.90	0.57	0.68

^a from [94]. ^b from [93]. ^c from [99] ^d from [95] ^e from [96].

Table 5 Barrier height for magnetization reversal U_{eff} (cm⁻¹) and energy gap between the two lowest Kramers doublets ΔE (cm⁻¹) in actinide single-molecule magnets ^a.

	U_{eff}	ΔE
$\text{U}(\text{Ph}_2\text{BPz}_2)_3$	20	190
$\text{U}(\text{H}_2\text{BPz}_2)_3$	16	230
$[\text{UTp}_3]$	3.8	270
$[\text{U}(\text{Tp}^{\text{Me}_2})_2(\text{bipy})]\text{I}$	18.2	137
$[\text{UTp Me}_2]\text{I}$	21.0	187
$[\text{U}(\text{H}_2\text{Bpz}_2)_3]$	16	108
$[\text{U}(\text{Bc}^{\text{Me}})_3]$	23	109
UTp_3	3.8	258
$[\text{U}(\text{BcMe}_3)_3]$	33	142
$\text{Np}(\text{COT})_2$	28.5	1400
PuTp_3	18.2	332

^a from [89, 99, 100].

8 U(IV) complexes

The U(IV) complexes with a $5f^2$ configuration are non-Kramers ions. The ground free-ion term 3H_4 might split into nine non-degenerate levels. In Section 5.2, we referred to an octahedral complex $[\text{U}^{\text{IV}}\text{F}_6]^{2-}$ with a non-degenerate ground state and TIP behavior [70], and in Section 5.3, to two pseudo-tetrahedral complexes $\text{U}^{\text{IV}}(\text{O})(\text{NSiMe}_3)_3]^-$ and $[\text{U}^{\text{IV}}\text{O}]^{2+}$ with a non-Kramers doublet for ground state [64].

The $(\text{C}_5\text{Me}_4\text{H})_3\text{U}^{\text{IV}}\text{NO}$, $(\text{C}_5\text{Me}_4\text{H})_3\text{U}^{\text{IV}}\text{Cl}$, $(\text{C}_5\text{H}_5)_3\text{U}^{\text{IV}}\text{CH}_3$, $(\text{C}_5\text{H}_5)_3\text{U}^{\text{IV}}\text{Cl}$ complexes have a three-fold symmetry. SO-CASPT2 calculations reveal a non-degenerate ground state of symmetry A_1 . With the NO^- ligand, there is a strong π interac-

tion and the first excited doublet lies at more than 4000 cm^{-1} leading to a TIP susceptibility in accordance with the experimental data. With Cl^- , the excited doublets are at 200 and 800 cm^{-1} , leading to more entangled contributions, which are correctly described by SO-CASPT2. Finally, with the CH_3^- ligand, all degeneracies are lifted and there are states equally distributed [101]. Finally, the susceptibility of the $[(\text{Tp}_2^*\text{U}^{\text{IV}})_2(p\text{-DIB})]$, $[(\text{Tp}_2^*\text{U}^{\text{IV}})_2(m\text{-DIB})]$, $[(\text{Tp}_2^*\text{U}^{\text{IV}})_2(\text{N-}p\text{-Tol})]$, $[(\text{Tp}_2^*\text{U}^{\text{IV}})\text{amidinate}]$ complexes are fitted by crystal-field parameters [92].

9 Pu(III) complexes

In $5f^5$ Pu(III) complexes, the ground term of the free ion $^6H_{5/2}$ splits in three Kramers doublets.

The $[\text{Pu}^{\text{III}}\text{Tp}_3]$ complex shows SMM properties with a barrier of 18.2 cm^{-1} . The first excited Kramers doublet is found to be at 332 or 400 cm^{-1} based on a crystal-field or SO-CASSCF analysis, respectively. SO-CASSCF leads to a TIP susceptibility, which does not fit the curvature of the experimental curve [102, 103]. The susceptibility of the Pu(III) ion in a matrix of LaPO_4 was measured by SQUID. The SO-CASSCF calculation performed on a $[\text{PuLa}_9(\text{PO}_4)_7]^{9+}$ cluster gives a first excited Kramers doublet at about 300 cm^{-1} . This leads to an almost linear χT which does not reproduce the experimental curve which reveals a pronounced curvature. The fitting of the experimental curve leads to a more compact spectrum, and the crystal-field strength parameter S is reduced from 500 to less than 200 cm^{-1} . Benchmark calculations on the $[\text{Pu}^{\text{III}}\text{Cl}_6]^{3-}$ complex show that an extended number of states should be included in the spin-orbit interaction, namely the spin doublets states, in order to approach the experimental energy gaps. It shows that the J-mixing in Pu(III) complexes is essential and completely changes the ordering of the states issued from the ground J manifold [104], as already mentioned for Pu(IV) complexes in Section 3.1.

10 Am(III) complexes

The $5f^6$ Am(III) free ion has a non-degenerate 7F_0 ground term. The susceptibility of the Am(III) ion was measured by SQUID in a matrix of LaPO_4 [104]. SO-CASPT2 retrieves this non-magnetic ground state with an excited state at 1600 cm^{-1} . The inclusion of the spin triplets in the spin-orbit interaction impacts strongly this gap. This leads to a pure TIP susceptibility behavior in good accordance with the magnetic data, except that the latter shows a small curvature.

11 Conclusion

In actinide complexes, the electron-electron repulsion, spin-orbit interaction and crystal-field effects are of about the same order of magnitude. It makes the description of their electronic structure and their magnetic properties, difficult, but challenging.

The electronic structure of symmetrical $5f^1$ complexes are rationalized by the singly-occupied one-electron wave-function, including crystal-field and spin-orbit, namely the singly-occupied spinor. The electronic structure of $5f^N$ is more tricky. In all cases, the crystal-field configuration before spin-orbit reveals a high-spin configuration, in favor of a weak-field coupling scheme. But the analysis in terms of spinors reveals configurations with doubly-occupied spinors. Clearly, the electronic structure should be grasped in an intermediate coupling scheme, between the LS coupling scheme where the many-electron wave-function is built and spin-orbit coupling calculated afterwards, and the j-j coupling where the spin-orbit is considered at the one-electron level. With many N electrons, it is difficult to figure out what the ground state is, without numerical tools. In those cases, the weight of the closed-shell spinors is non negligible. An e^2 configuration where e is a two-fold spinor has non magnetic contribution, the spin and orbital contributions from the components e and \bar{e} cancel each other, but arises from spin-singlet and spin-triplet contributions. It shows that all spin-states should be included in the spin-orbit state interaction, as for example spin-doublets for Pu(III) complexes.

SO-CAS methods are, at the present time, the most suitable methods to describe the electronic structure of actinide complexes, and their magnetic properties. Indeed, those methods include in the calculation the three ingredients, the electron-electron repulsion, spin-orbit interaction and crystal-field effects, in a balanced way. At first, the orbitals are built (crystal-field), then the many-electron wave-function (electron-electron repulsion) and finally, the spin-orbit as a state interaction. This follows the LS coupling scheme. For $5f^1$ complexes, DFT methods including spin-orbit interaction are suitable, but sometimes converge to a wrong state.

The magnetization of doublet states can be characterized by the g-tensors. The comparison of the ab initio g-factors with the experimental ones, usually determined by EPR spectroscopy shows a good agreement. It shows that SO-CAS based methods provide the correct ground state, even at SO-CASSCF level.

Crystal-field theory allows to describe the splitting of the seven 5f orbitals by the ligands. Due to a larger covalency as compared to the lanthanide counterparts, the effects are much larger in actinide complexes. The crystal-field parameters deduced from the ground J-multiplet include in an effective way many-electron and spin-orbit interactions, and are different from the one-electron values. And this, specially for Pu complexes, where the J-mixing shakes up the components issued from this J-multiplet.

The magnetic susceptibility probes many states, either populated contributing to the Curie term, or not, adding a temperature independent term (TIP). In actinide complexes, the overall splitting of the ground J-multiplet is more than 1000 cm^{-1} . Some of the states are not populated at room temperature, but have a non-negligible contribution through the TIP mechanism. If some of the states lie in the 200 - 600

cm^{-1} window, the thermal expansion should include further terms in T^{-n} to the Curie law. The χT as a function of T is sensitive to many parameters: the energy of the states, the magnetic moments of the degenerate manifolds and the magnetic coupling between those manifolds. SO-CAS based methods sometimes fit well the experimental curves. But sometimes, they do not fit so well. The agreement is usually improved by including the dynamical correlation, with CASPT2 or NEVPT2 methods, or/and to increase the size of the active space by including some bonding orbitals of the ligands or the 6d orbitals.

To conclude, the interplay of experimental data, model Hamiltonians and first-principle description allows to approach the electronic structure of actinide complexes and their magnetic properties, with or without symmetry, with one or more electrons in the 5f shell.

Acknowledgements This text has largely benefited from fruitful collaborations over the time: François-Paul Notter, Talal Mallah, Claude Berthon, Jochen Autschbach, Florian Koprowiak, Matthieu Autillo, Frédéric Gendron, Md. Ashraful Islam. I deeply thank all of them for the richness of our scientific discussions.

Appendices

A Generalized Van Vleck equation

The magnetic susceptibility tensor χ at temperature T is expressed as the thermal Boltzmann average according to the eigenfunctions of $\hat{\mathcal{H}}$ and the corresponding magnetic moments as

$$\chi_{uv} = -\mathcal{N}_A \mu_0 \mu_B \frac{\sum_{I,\iota} M_{I,\iota,uv}(B_u) e^{-\frac{E_{I,\iota}(B_u)}{kT}}}{B_u \sum_{I,\iota} e^{-\frac{E_{I,\iota}(B_u)}{kT}}} \quad (\text{A1})$$

To derive the Van Vleck equation, the Zeeman interaction is considered perturbatively and the zeroth-order states $|I, \iota\rangle$ are eigenstates of $\hat{\mathcal{H}}^0$ with energy E_I^0 . ι runs over the components of degenerate manifolds. The angular momentum operator $\hat{\mathbf{M}}$ is a time-odd operator, leading to specific properties [40, 105]. In a degenerate manifold I ,

$$\sum_{\iota} \langle I, \iota | \hat{M}_u | I, \iota \rangle = 0 \quad (\text{A2})$$

In Eq. 4, $M_{I,\iota,uv}(B_u)$ is the angular momentum of state I in direction u for a magnetic field applied in direction v . The perturbative Hamiltonian is given by $\hat{\mathcal{H}}^Z = \mu_B \hat{M}_u B_u$. To apply perturbation theory in degenerate manifolds, the $|I, \iota\rangle$ are considered to be eigenfunctions of the perturbative Hamiltonian, depending consequently on the direction of the field. At second order of perturbation theory, the eigenstates are

$$\chi_{uv} = \mathcal{N}_A \frac{d^2 E}{dB_u dB_v} \quad (\text{A10})$$

which leads to Eq. A8 in the case of perturbation theory of degenerate states.

The matrix representation \mathbf{M}_u of $\hat{\mathbf{M}}_u$ in the basis of the zero-field states $|I, \iota\rangle$ may be decomposed in block matrices within degenerate zero-field manifolds: the diagonal blocks $\mathbf{M}_{u,I}$ within manifold I , and the off-diagonal blocks $\mathbf{M}_{u,IK}$ coupling the two manifolds I and K

$$\mathbf{M}_u = \begin{bmatrix} \mathbf{M}_{u,1} & \cdots & \mathbf{M}_{u,1N} \\ \vdots & \ddots & \vdots \\ \mathbf{M}_{u,N1} & \cdots & \mathbf{M}_{u,N} \end{bmatrix} \quad (\text{A11})$$

Eq. A8 becomes

$$\chi_{uv} = \mathcal{N}_A \mu_0 \mu_B^2 \frac{1}{Q_0} \sum_I e^{-\frac{E_I^0}{kT}} \left[\frac{1}{kT} \text{tr} \left(\mathbf{M}_{u,I} \cdot \mathbf{M}_{v,I}^\dagger \right) + 2 \sum_{K \neq I} \frac{\text{tr} \left(\mathbf{M}_{u,IK} \cdot \mathbf{M}_{v,IK}^\dagger \right)}{E_J^0 - E_I^0} \right] \quad (\text{A12})$$

where tr denotes the trace of a matrix. For the diagonal components, $u = v$, $\text{tr} \left(\mathbf{M}_{u,IK} \cdot \mathbf{M}_{u,IK}^\dagger \right) = \sum_{\iota, \kappa} \left\langle I, \iota \left| \hat{M}_u \right| K, \kappa \right\rangle^2 = \|\mathbf{M}_{u,IK}\|^2$ where $\|\cdot\|$ denotes the norm of the matrix. One gets

$$\chi_{uu} = \mathcal{N}_A \mu_0 \mu_B^2 \frac{1}{Q_0} \sum_I e^{-\frac{E_I^0}{kT}} \left[\frac{\|\mathbf{M}_{u,I}\|^2}{kT} + 2 \sum_{K \neq I} \frac{\|\mathbf{M}_{u,IK}\|^2}{E_K^0 - E_I^0} \right] \quad (\text{A13})$$

The sum is now over the degenerate manifolds of the zero-field Hamiltonian.

B Tables

Table A1 f orbitals in linear symmetry.

ω	spherical harmonics	Cartesian
σ	$r^3 Y_3^0$	$\sqrt{\frac{7}{16\pi}} z (5z^2 - 3r^2)$
π_1	$r^3 \frac{Y_3^1 + Y_3^{-1}}{\sqrt{2}} * i$	$\sqrt{\frac{7}{16\pi}} \sqrt{\frac{3}{2}} y (5z^2 - r^2)$
π_2	$r^3 \frac{Y_3^1 - Y_3^{-1}}{\sqrt{2}} * (-1)$	$\sqrt{\frac{7}{16\pi}} \sqrt{\frac{3}{2}} x (5z^2 - r^2)$
δ_1	$r^3 \frac{Y_3^2 + Y_3^{-2}}{\sqrt{2}}$	$\sqrt{\frac{7}{16\pi}} \sqrt{15} (zx^2 - zy^2)$
δ_2	$r^3 \frac{Y_3^2 - Y_3^{-2}}{\sqrt{2}i}$	$\sqrt{\frac{7}{16\pi}} 2\sqrt{15}xyz$
ϕ_1	$r^3 \frac{Y_3^3 + Y_3^{-3}}{\sqrt{2}} * i$	$\sqrt{\frac{7}{16\pi}} \sqrt{\frac{5}{2}} (3x^2y - y^3)$
ϕ_2	$r^3 \frac{Y_3^3 - Y_3^{-3}}{\sqrt{2}} * (-1)$	$\sqrt{\frac{7}{16\pi}} \sqrt{\frac{5}{2}} (x^3 - 3xy^2)$

Table A2 f orbitals in cubic symmetries.

\mathcal{O}_h	\mathcal{T}_d				Cartesian
a_{2u}	a_1		δ_2		$\sqrt{\frac{7}{16\pi}} 2\sqrt{15}xyz$
t_{1u}	t_2	x^3	$-\frac{\sqrt{3}}{2\sqrt{2}}\pi_2 + \frac{\sqrt{5}}{2\sqrt{2}}\phi_2$		$\sqrt{\frac{7}{16\pi}} x(5x^2 - 3r^2)$
		y^3	$-\frac{\sqrt{3}}{2\sqrt{2}}\pi_1 - \frac{\sqrt{5}}{2\sqrt{2}}\phi_1$		$\sqrt{\frac{7}{16\pi}} y(5y^2 - 3r^2)$
		z^3	σ		$\sqrt{\frac{7}{16\pi}} z(5z^2 - 3r^2)$
t_{2u}	t_1	$x(y^2 - z^2)$	$-\frac{\sqrt{5}}{2\sqrt{2}}\pi_2 - \frac{\sqrt{3}}{2\sqrt{2}}\phi_2$		$\sqrt{\frac{7}{16\pi}} \sqrt{15}x(y^2 - z^2)$
		$y(z^2 - x^2)$	$\frac{\sqrt{5}}{2\sqrt{2}}\pi_1 - \frac{\sqrt{5}}{2\sqrt{2}}\phi_1$		$\sqrt{\frac{7}{16\pi}} \sqrt{15}y(z^2 - x^2)$
		$z(x^2 - y^2)$	δ_1		$\sqrt{\frac{7}{16\pi}} \sqrt{15}z(x^2 - y^2)$

Table A3 Spin-orbit operator in the f spin-orbitals basis.

$\hat{\mathbf{l}} \cdot \hat{\mathbf{s}}$		$ \sigma\rangle$	$ \bar{\pi}_1\rangle$	$ \bar{\pi}_2\rangle$	$ \delta_1\rangle$	$ \delta_2\rangle$	$ \bar{\phi}_1\rangle$	$ \bar{\phi}_2\rangle$
		$ \bar{\sigma}\rangle$	$ \pi_1\rangle$	$ \pi_2\rangle$	$ \bar{\delta}_1\rangle$	$ \bar{\delta}_2\rangle$	$ \phi_1\rangle$	$ \phi_2\rangle$
$\langle\sigma $	$\langle\bar{\sigma} $	0	-2μ	$-i2\mu$	0	0	0	0
$\langle\bar{\pi}_1 $	$\langle\pi_1 $	-2μ	0	$-\frac{i}{2}$	ν	$-i\nu$	0	0
$\langle\bar{\pi}_2 $	$\langle\pi_2 $	$i2\mu$	$\frac{i}{2}$	0	$i\nu$	ν	0	0
$\langle\delta_1 $	$\langle\bar{\delta}_1 $	0	ν	$-i\nu$	0	i	$-\mu$	$-i\mu$
$\langle\delta_2 $	$\langle\bar{\delta}_2 $	0	$i\nu$	ν	$-i$	0	$i\mu$	$-\mu$
$\langle\bar{\phi}_1 $	$\langle\phi_1 $	0	0	0	$-\mu$	$-i\mu$	0	$-\frac{3i}{2}$
$\langle\bar{\phi}_2 $	$\langle\phi_2 $	0	0	0	$i\mu$	$-\mu$	$\frac{3i}{2}$	0

$\mu = \frac{\sqrt{3}}{2\sqrt{2}}; \nu = \frac{\sqrt{5}}{2\sqrt{2}}$

Table A4 \hat{l}_u operators in the f spin-orbitals basis.

\hat{l}_x		$ \sigma\rangle$	$ \pi_1\rangle$	$ \pi_2\rangle$	$ \delta_1\rangle$	$ \delta_2\rangle$	$ \phi_1\rangle$	$ \phi_2\rangle$
		$ \bar{\sigma}\rangle$	$ \bar{\pi}_1\rangle$	$ \bar{\pi}_2\rangle$	$ \bar{\delta}_1\rangle$	$ \bar{\delta}_2\rangle$	$ \bar{\phi}_1\rangle$	$ \bar{\phi}_2\rangle$
$\langle\sigma $	$\langle\bar{\sigma} $	0	$i\sqrt{6}$	0	0	0	0	0
$\langle\pi_1 $	$\langle\bar{\pi}_1 $	$-i\sqrt{6}$	0	0	$-i2\nu$	0	0	0
$\langle\pi_2 $	$\langle\bar{\pi}_2 $	0	0	0	0	$i2\nu$	0	0
$\langle\delta_1 $	$\langle\bar{\delta}_1 $	0	$i2\nu$	0	0	0	$i2\mu$	0
$\langle\delta_2 $	$\langle\bar{\delta}_2 $	0	0	$-i2\nu$	0	0	0	$-i2\mu$
$\langle\phi_1 $	$\langle\bar{\phi}_1 $	0	0	0	$-i2\mu$	0	0	0
$\langle\phi_2 $	$\langle\bar{\phi}_2 $	0	0	0	0	$i2\mu$	0	0

\hat{l}_y		$ \sigma\rangle$	$ \pi_1\rangle$	$ \pi_2\rangle$	$ \delta_1\rangle$	$ \delta_2\rangle$	$ \phi_1\rangle$	$ \phi_2\rangle$
		$ \bar{\sigma}\rangle$	$ \bar{\pi}_1\rangle$	$ \bar{\pi}_2\rangle$	$ \bar{\delta}_1\rangle$	$ \bar{\delta}_2\rangle$	$ \bar{\phi}_1\rangle$	$ \bar{\phi}_2\rangle$
$\langle\sigma $	$\langle\bar{\sigma} $	0	0	$i\sqrt{6}$	0	0	0	0
$\langle\pi_1 $	$\langle\bar{\pi}_1 $	0	0	0	0	$i2\nu$	0	0
$\langle\pi_2 $	$\langle\bar{\pi}_2 $	$-i\sqrt{6}$	0	0	$i2\nu$	0	0	0
$\langle\delta_1 $	$\langle\bar{\delta}_1 $	0	0	$-i2\nu$	0	0	0	$i2\mu$
$\langle\delta_2 $	$\langle\bar{\delta}_2 $	0	$-i2\nu$	0	0	0	$i2\mu$	0
$\langle\phi_1 $	$\langle\bar{\phi}_1 $	0	0	0	0	$-i2\mu$	0	0
$\langle\phi_2 $	$\langle\bar{\phi}_2 $	0	0	0	$-i2\mu$	0	0	0

\hat{l}_z	$ \sigma\rangle$ $ \bar{\sigma}\rangle$	$ \pi_1\rangle$ $ \bar{\pi}_1\rangle$	$ \pi_2\rangle$ $ \bar{\pi}_2\rangle$	$ \delta_1\rangle$ $ \bar{\delta}_1\rangle$	$ \delta_2\rangle$ $ \bar{\delta}_2\rangle$	$ \phi_1\rangle$ $ \bar{\phi}_1\rangle$	$ \phi_2\rangle$ $ \bar{\phi}_2\rangle$
$\langle\sigma $	$\langle\bar{\sigma} $	0	0	0	0	0	0
$\langle\pi_1 $	$\langle\bar{\pi}_1 $	0	0	i	0	0	0
$\langle\pi_2 $	$\langle\bar{\pi}_2 $	0	$-i$	0	0	0	0
$\langle\delta_1 $	$\langle\bar{\delta}_1 $	0	0	0	0	$-2i$	0
$\langle\delta_2 $	$\langle\bar{\delta}_2 $	0	0	0	$2i$	0	0
$\langle\phi_1 $	$\langle\bar{\phi}_1 $	0	0	0	0	0	$3i$
$\langle\phi_2 $	$\langle\bar{\phi}_2 $	0	0	0	0	$-3i$	0

References

1. L. Morss, N.M. Edelstein, J. Fuger (eds.), *The chemistry of the actinide and transactinide elements* (Springer, The Netherlands, 2010)
2. F. Gendron, J. Autschbach, in *Encyclopedia of Inorganic and Bioinorganic Chemistry*, ed. by R. Scott (2018), pp. 1–16
3. N. Kaltsoyannis, P.J. Hay, J. Li, J.P. Blaudeau, B.E. Bursten, in *The chemistry of the actinide and transactinide elements*, 4th ed., vol. 3, ed. by L. Morss, N.M. Edelstein, J. Fuger (Springer, The Netherlands, 2010), p. 1893
4. N. Kaltsoyannis, *Chem. Eur. J.* **24**, 2815 (2018)
5. F. Neese, *ChemChysChem* **12**, 3077 (2011)
6. T. Saue, L. Visscher, *Relativistic all-electron approaches to the study of element chemistry* (John Wiley and Sons, Ltd, 2015), pp. 55–87
7. B.O. Roos, P.Å. Malmqvist, *Phys. Chem. Chem. Phys.* **6**, 2919 (2004)
8. B.O. Roos, P.R. Taylor, P.E.M. Siegbahn, *Chem. Phys.* **48**, 157 (1980)
9. K. Andersson, P.A. Malmqvist, B.O. Roos, A.J. Sadlej, K. Wolinski, *J. Phys. Chem.* **94**, 5483 (1990)
10. C. Angeli, R. Cimiraglia, J.P. Malrieu, *J. Chem. Phys.* **117**(20), 9138 (2002). DOI 10.1063/1.1515317
11. P.A. Malmqvist, B.O. Roos, B. Schimmelpfennig, *Chem. Phys. Lett.* **357**, 230 (2002)
12. J.B. Rota, S. Knecht, T. Fleig, D. Ganyushin, T. Saue, F. Neese, H. Bolvin, *J. Chem. Phys.* p. 114106 (2011)
13. S. Knecht, H.J.A. Jensen, T. Saue, *Nat. Comm.* **11**, 40 (2018)
14. S. Vancoillie, F. Neese, L. Rulisek, K. Pierloot, *J. Phys. Chem. A* **113**, 6149 (2009)
15. D. Evans, *J. Chem. Soc.* pp. 2003–2005 (1959)
16. M. Gerloch, R.F. McMeeking, *J. Chem. Soc., Dalton Trans.* pp. 2443–2451 (1975)
17. R. Boča, *Theoretical foundations of molecular magnetism* (Elsevier, Amsterdam, 1999)
18. O. Kahn, *Molecular magnetism* (Wiley-VCH, New-York, 1993)
19. D.R. Kindra, W.J. Evans, *Chem. Rev.* **114**, 8865 (2014)
20. T.F. Wall, J. Steve, M. Autillo, L. Nash, K., L. Guerin, C. Le Naour, P. Moisy, C. Berthon, *Inorg. Chem.* **53**, 2450 (2014). DOI 10.1021/ic402371x
21. C. Apostolidis, B. Schimmelpfennig, N. Magnani, P. Lindqvist-Reis, O. Walter, R. Sykora, A. Morgenstern, E. Colineau, R. Caciuffo, R. Klenze, R. Haire, J. Rebizant, F. Bruchertseifer, T. Fangh"anel, *Angew. Chem. Int. Ed.* **49**, 6343 (2010)
22. M. Autillo, L. Guerin, D. Guillaumont, P. Moisy, H. Bolvin, C. Berthon, *Inorg. Chem.* **55**, 12149 (2016)

23. M. Autillo, L. Guerin, H. Bolvin, P. Moisy, C. Berthon, *Phys. Chem. Chem. Phys.* **18**, 6515 (2016)
24. H. Schilder, H. Lueken, J. Magn. Mater. **281**, 17 (2004)
25. N.F. Chilton, R.P. Anderson, L.D. Turner, A. Soncini, K.S. Murray, *J. Comput. Chem.* **34**, 1164 (2013)
26. L.F. Chibotaru, N. Iwahara, *New J. Phys.* **17**, 103028 (2015)
27. F. Koprowiak, Etude théorique de l'anisotropie magnétique dans des dimères d'éléments f. Ph.D. thesis, Université de Toulouse, Toulouse (2017)
28. L. Belkhiri, B. Le Guennic, A. Boucekkine, *Magnetochemistry* **5** (2019)
29. J.S. Griffith, *The theory of transition metal ions* (Cambridge University Press, Cambridge, 1961)
30. J. van Leusen, M. Speldrich, H. Schilder, P. Kögerler, *Coordin. Chem. Rev.* **289-290**, 137 (2015)
31. M. Atanasov, D. Ganyushin, K. Sivalingam, F. Neese, *Structure and Bonding, A Modern First-Principles View on Ligand Field Theory Through the Eyes of Correlated Multireference Wavefunctions*. (Springer, Berlin, Heidelberg, 2011), vol. 143, pp. 149–220
32. C. Rudowicz, M. Karbowiak, *Coordin. Chem. Rev.* **287**, 28 (2015)
33. J. van Leusen, M. Speldrich, P. Kögerler, *Magnetism of Actinide Coordination Compounds* (Springer International Publishing, Cham, 2019), pp. 391–410
34. J.P. Malrieu, R. Caballol, C.J. Calzado, C. de Graaf, N. Guihéry, *Chem. Rev.* **114**, 429 (2014)
35. D. Páez Hernández, H. Bolvin, *J. Electron. Spectrosc. Relat. Phenom.* **194**, 74 (2014)
36. L. Ungur, L.F. Chibotaru, *Chem. Eur. J.* **23**, 3708 (2017)
37. R. Alessandri, H. Zulfikri, J. Autschbach, H. Bolvin, *Chem. Eur. J.* **24**, 5538 (2018)
38. G. Racah, *Phys. Rev.* **76**, 1652 (1949)
39. K.W.H. Stevens, *Proc. phys. Soc. A* **65**, 209 (1952)
40. A. Abragam, B. Bleaney, *Electronic paramagnetic resonance of transition ions* (Clarendon Press, Oxford, 1970)
41. B.G. Wybourne, *Spectroscopic Properties of Rare Earths* (Wiley-Interscience, New-York, 1965)
42. C. Görlner-Walrand, K. Binnemans, *Chapter 155 Rationalization of crystal-field parametrization* (Elsevier, 1996), vol. 23, pp. 121 – 283
43. M. Atanasov, J.M. Zadrozny, J.R. Long, F. Neese, *Chem. Sci.* **4**, 139 (2013)
44. J. Jung, M.A. Islam, V.L. Pecoraro, T. Mallah, C. Berthon, H. Bolvin, *Chem. Eur. J.* **25**, 15112 (2019)
45. N.C. Chang, J.B. Gruber, R.P. Leavitt, C.A. Morrison, *J. Chem. Phys.* **76**, 3877 (1982)
46. M. Karbowiak, C. Rudowicz, *Polyhedron* **93**, 91 (2015)
47. L. Chibotaru, L. Ungur, *J. Chem. Phys.* **137**, 064112 (2012)
48. H. Bolvin, J. Autschbach, *Handbook of relativistic quantum chemistry* (Springer, Berlin, 2017), chap. Relativistic methods for calculating Electron Paramagnetic Resonance (EPR) parameters
49. H. Bolvin, *ChemPhysChem* **7**, 1575 (2006)
50. J.S. Griffith, *Phys. Rev.* **132**, 316 (1963)
51. B. Bleaney, *Proc. Phys. Soc. Lond.* **73**, 939 (1959)
52. M. Autillo, M.A. Islam, J. Héron, L. Guérin, E. Acher, C. Tamain, M.C. Illy, P. Moisy, E. Colineau, J.C. Griveau, C. Berthon, H. Bolvin, *Chem. Eur. J.* **27**, 7138 (2021)
53. J.C. Eisenstein, M.H.L. Pryce, *Proc. Roy. Soc. London A* **229**, 20 (1955)
54. F. Gendron, D. Páez Hernández, F.P. Notter, B. Pritchard, H. Bolvin, J. Autschbach, *Chem. Eur. J.* **20**, 7994 (2014)
55. D.M. King, P.A. Cleaves, A.J. Wooles, B.M. Gardner, N.F. Chilton, F. Tuna, W. Lewis, E.J.L. McInnes, S.T. Liddle, *Nat. commun.* **7**, 13773 (2016)
56. A.F. Leung, E. Wong, *Phys. Rev.* **187**(2), 504 (1969). DOI 10.1103/PhysRev.187.504
57. R.G. Denning, J.O.W. Norris, D. Brown, *Mol. Phys.* **46**, 287 (1982)
58. M.H.L. Pryce, *Phys. Rev. Lett.* **3**, 375 (1959)
59. A.F. Leung, E.Y. Wong, *Phys. Rev.* **180**(2), 380 (1969). DOI 10.1103/PhysRev.180.380

60. F. Gendron, B. Pritchard, H. Bolvin, J. Autschbach, *Dalton Trans.* p. 19886 (2015)
61. F. Gendron, H. Bolvin, J. Autschbach, *Complete Active Space Wavefunction-Based Analysis of Magnetization and Electronic Structure* (Springer International Publishing, Cham, 2019), pp. 355–390
62. J.C. Eisenstein, M.H.L. Pryce, *Proc. Roy. Soc. London A* **238**, 31 (1956)
63. F. Gendron, B. Pritchard, H. Bolvin, J. Autschbach, *Inorg. Chem.* **53**, 8577 (2014)
64. J.A. Seed, L. Birnoschi, E.L. Ashley, J. Woole, N.F. Chilton, S.T. Liddle, *Chem* **7** (2021)
65. F. Notter, S. Dubillard, H. Bolvin, *J. Chem. Phys.* **128**, 164315 (2008)
66. J.C. Eisenstein, M.H.L. Pryce, *Proc. R. Soc. Lond. A* **255**, 181 (1960)
67. F.P. Notter, H. Bolvin, *J. Chem. Phys.* **130**, 184310 (2009)
68. F. Gendron, V.E. Fleischauer, T.J. Duignan, B.L. Scott, M.W. Löble, S.K. Cary, S.A. Kozimor, H. Bolvin, M.L. Neidig, J. Autschbach, *Phys. Chem. Chem. Phys.* **19**, 17300 (2017)
69. F. RWihelm, J.P. Sanchez, A. Rogalev, *J. Phys. D: Appl. Phys.* **51**, 333001 (2018)
70. K.S. Pedersen, K.R. Meihaus, A. Rogalev, F. Wilhelm, D. Aravena, M. Amoa, E. Ruiz, J.R. Long, J. Bendix, R. Clérac, *Angew. Chem. Int. Ed.* **58**, 15650 (2019)
71. E. Hashem, J.A. Platts, F. Hartl, G. Lorusso, M. Evangelisti, C. Schulzke, R.J. Baker, *Inorg. Chem.* **53**, 8624 (2014)
72. F. Gendron, J. Autschbach, *J. Phys. Chem. Lett.* **8**, 673 (2017)
73. M. Viciano-Chumillas, F. Koprowiak, I. Mutikainen, W. Wernsdorfer, T. Mallah, H. Bolvin, *Phys. Rev. B* **96**, 214427 (2017)
74. K.D. Warren, *Inorg. Chem.* **14**, 3095 (1975)
75. F. Gendron, J. Autschbach, J. Malrieu, H. Bolvin, *Inorg. Chem.* **58**, 581 (2019)
76. D. Gourier, D. Caurant, T. Arliguie, M. Ephritikhine, *J. Am. Chem. Soc.* **120**, 6084 (1998)
77. D.C. Sergentu, F. Gendron, J. Autschbach, *Chem. Sci.* **9**, 6292 (2018)
78. Y. Qiao, G. Ganguly, C.H. Booth, J.A. Branson, A.S. Ditter, D.J. Lussier, L.M. Moreau, D.R. Russo, D.C. Sergentu, D.K. Shuh, T. Sun, J. Autschbach, S.G. Minasian, *Chem. Commun.* **57**, 9562 (2021)
79. N. Rösch, A.J. Streitwieser, *J. Am. Chem. Soc.* **105**, 7237 (1983)
80. R.J. Strittmatter, B.E. Bursten, *J. Am. Chem. Soc.* **113**, 552 (1991)
81. M. Dolg, P. Fulde, H. Stoll, H. Preuss, A. Chang, R.M. Pitzer, *Chem. Phys.* **195**, 71 (1995)
82. D.J.A. De Ridder, J. Rebizant, C. Apostolidis, B. Kanellakopulos, E. Dornberger, *Acta Cryst. C* **52**, 597 (1996)
83. J. Li, B.E. Bursten, *J. Am. Chem. Soc.* **119**(38), 9021 (1997)
84. G. Hong, F. Schautz, M. Dolg, *J. Am. Chem. Soc.* **121**, 1502 (1999)
85. N. Magnani, C. Apostolidis, A. Morgenstern, E. Colineau, J.C. Griveau, H. Bolvin, O. Walter, R. Caciuffo, *Angew. Chem. Int. Ed.* **50**, 1696 (2011)
86. E. Solis-Céspedes, D. Pérez Hernández, *Dalton Trans.* **46**, 4834 (2017)
87. S.K. Singh, C.J. Cramer, L. Gagliardi, *Inorg. Chem.* **59**, 6815 (2020)
88. S. Dey, G. Rajaraman, *J. Chem. Sci.* **131**, 124 (2019)
89. K.R. Meihaus, J.R. Long, *Dalton Trans.* **44**, 2517 (2015)
90. C. Apostolidis, A. Morgenstern, J. Rebizant, B. Kanellakopulos, O. Walter, B. Powietzka, M. Karbowiak, H. Reddmann, H.D. Amberger, Z. Anorg. Allg. Chem. **636**, 201 (2010)
91. J.J. Baldoví, S. Cardona-Serra, J.M. Clemente-Juan, E. Coronado, A. Gaita-Ariño, *Chem. Sci.* **4**, 938 (2013)
92. R.F. Higgins, C.J. Tatebe, S.C. Bart, M.P. Shores, *Chem. Commun.* **55**, 10611 (2019)
93. A. Formanuk, A.M. Ariciu, F. Ortu, R. Beekmeyer, A. Kerridge, F. Tuna, E.J.L. McInnes, D.P. Mills, *Nat. Chem.* **9**, 578 (2017)
94. W.W. Lukens, M. Speldrich, P. Yang, T.J. Duignan, J. Autschbach, P. Kögerler, *Dalton Trans.* **45**, 11508 (2016)
95. J.T. Coutinho, M. Perfetti, J.J. Baldoví, M.A. Antunes, P.P. Hallmen, H. Bamberger, I. Crassee, M. Orlita, M. Almeida, J. van Slageren, L.C.J. Pereira, *Chem. Eur. J.* **25**, 1758 (2019)
96. N.J. Wolford, X. Yu, S.C. Bart, J. Autschbach, M.L. Neidig, *Dalton Trans.* **49**, 14401 (2020)
97. M.A. Antunes, L.C.J. Pereira, I.C. Santos, M. Mazzanti, J. Marcalo, M. Almeida, *Inorg. Chem.* **50**, 9915 (2011)

98. J.T. Coutinho, M.A. Antunes, L.C.J. Pereira, H. Bolvin, J. Marçaloa, M. Mazzanti, M. Almeida, Dalton Trans **41**, 13568 (2012)
99. M. Spivak, K.D. Vogiatzis, C.J. Cramer, C.d. Graaf, L. Gagliardi, J. Phys. Chem. A **121**(8), 1726 (2017)
100. S. Dey, G. Velmurugan, G. Rajaraman, Dalton Trans. **48**, 8976 (2019)
101. F. Gendron, B. Le Guennic, J. Autschbach, Inorg. Chem. **53**, 13174 (2014)
102. N. Magnani, E. Colineau, J.C. Griveau, C. Apostolidis, O. Walter, R. Caciuffo, Chem. Commun. **50**, 8171 (2014)
103. C.A. Gaggioli, L. Gagliardi, Inorg. Chem. **57**, 8098 (2018)
104. L. Martel, M.A. Islam, K. Popa, J.F. Vigier, E. Colineau, H. Bolvin, J.C. Griveau, J. Phys. Chem. C **125**, 22163 (2021)
105. L.D. Barron, A.D. Buckingham, Acc. Chem. Res. **34**, 781 (2001)
106. J. Autschbach, *Quantum theory for chemical applications* (Oxford, University Press, Oxford, 2021)